


Conditional Astrocyte Rac1KO Attenuates Hyperreflexia after Spinal Cord Injury

Curtis A. Benson,^{1,2} Kai-Lan Olson,^{1,2} Siraj Patwa,^{1,2} Sierra D. Kauer,^{1,2} Jared F. King,^{1,2}  Stephen G. Waxman,^{1,2} and Andrew M. Tan^{1,2}

¹Department of Neurology and Center for Neuroscience and Regeneration Research, Yale University School of Medicine, New Haven, Connecticut 06510, and ²Rehabilitation Research Center, Veterans Affairs Connecticut Healthcare System, West Haven, Connecticut 06516

Spasticity is a hyperexcitability disorder that adversely impacts functional recovery and rehabilitative efforts after spinal cord injury (SCI). The loss of evoked rate-dependent depression (RDD) of the monosynaptic H-reflex is indicative of hyperreflexia, a physiological sign of spasticity. Given the intimate relationship between astrocytes and neurons, that is, the tripartite synapse, we hypothesized that astrocytes might have a significant role in post-injury hyperreflexia and plasticity of neighboring neuronal synaptic dendritic spines. Here, we investigated the effect of selective Rac1KO in astrocytes (i.e., adult male and female mice, transgenic cre-flox system) on SCI-induced spasticity. Three weeks after a mild contusion SCI, control Rac1^{WT} animals displayed a loss of H-reflex RDD, that is, hyperreflexia. In contrast, transgenic animals with astrocytic Rac1KO demonstrated near-normal H-reflex RDD similar to pre-injury levels. Reduced hyperreflexia in astrocytic Rac1KO animals was accompanied by a loss of thin-shaped dendritic spine density on α -motor neurons in the ventral horn. In SCI-Rac1^{WT} animals, as expected, we observed the development of dendritic spine dysgenesis on α -motor neurons associated with spasticity. As compared with WT animals, SCI animals with astrocytic Rac1KO expressed increased levels of the glial-specific glutamate transporter, glutamate transporter-1 in the ventral spinal cord, potentially enhancing glutamate clearance from the synaptic cleft and reducing hyperreflexia in astrocytic Rac1KO animals. Taken together, our findings show for the first time that Rac1 activity in astrocytes can contribute to hyperreflexia underlying spasticity following SCI. These results reveal an opportunity to target cell-specific molecular regulators of H-reflex excitability to manage spasticity after SCI.

Key words: astrocytes; dendritic spines; Rac1; spasticity; spinal cord injury

Significance Statement

Spinal cord injury leads to stretch reflex hyperexcitability, which underlies the clinical symptom of spasticity. This study shows for the first time that astrocytic Rac1 contributes to the development of hyperreflexia after SCI. Specifically, astrocytic Rac1KO reduced SCI-related H-reflex hyperexcitability, decreased dendritic spine dysgenesis on α -motor neurons, and elevated the expression of the astrocytic glutamate transporter-1 (GLT-1). Overall, this study supports a distinct role for astrocytic Rac1 signaling within the spinal reflex circuit and the development of SCI-related spasticity.

Introduction

A common consequence of spinal cord injury (SCI) is clinically significant spasticity, which can disrupt rehabilitation and negatively impact quality of life (Skold et al., 1999; Walter et al., 2002;

Holtz et al., 2017). A key mechanism driving spasticity after SCI is α -motor neuron hyperexcitability within the spinal stretch reflex circuit (H-reflex; Lance, 1980). Multiple factors have been implicated in H-reflex and motor neuron hyperexcitability including loss of descending cortical and local spinal segment inhibition; ion channel misexpression, for example, KCC2; and maladaptive CNS plasticity (Finnerup, 2017). Astrocytes also react to SCI and have the capacity to alter synaptic and circuit excitability (Blanco-Suárez et al., 2017; Andersen et al., 2021). In this study, we reasoned that targeting the neuron–astrocyte relationship might provide an effective strategy to reduce motor neuron hyperexcitability and spasticity associated with SCI (Tan et al., 2011; Tan and Waxman, 2012).

The tripartite synapse consists of the astrocytic process, post-synaptic dendritic spine, and pre-synaptic terminal. This concept

Received Sept. 1, 2022; revised Aug. 24, 2023; accepted Sept. 19, 2023.

Author contributions: C.B., K.O., S.W., and A.T. designed research; C.B., K.O., S.P., and S.K. performed research; C.B. analyzed data; C.B. and A.T. wrote the paper.

This work was supported by grants from the Paralyzed Veterans of America (PVA), the Department of Veterans Affairs (VA) Medical Research Service and Rehabilitation Research Service, and The Taylor Foundation for Chronic Disease. The Center for Neuroscience and Regeneration Research is a Collaboration of the Paralyzed Veterans of America with Yale University. We thank Jennifer Carrara and Pamela Zwinger for their excellent technical assistance.

The authors declare no competing financial interests.

Correspondence should be addressed to Andrew M. Tan at andrew.tan@yale.edu.

<https://doi.org/10.1523/JNEUROSCI.1670-22.2023>

Copyright © 2023 the authors

of a three-part synapse arose from the close contact and bidirectional signaling between neurons and astrocytes (Ventura and Harris, 1999; Savtchouk and Volterra, 2018). Astrocytes can detect extrasynaptic glutamate triggering astrocytic Ca^{2+} elevation that results in a variety of cellular processes including the release of signaling molecules, structural reorganization, and increased glutamate reuptake (Savtchouk and Volterra, 2018; Verkhratsky and Nedergaard, 2018). In the latter, astrocytes express GLT-1, which contributes to homeostatic clearance and recycling of glutamate from the synaptic cleft (Peterson and Binder, 2020). Impaired astrocytic GLT-1 leads to an accumulation of free glutamate levels within the synapse and abnormal postsynaptic AMPA and NMDA receptor signaling (Ji and Strichartz, 2004; Hefferan et al., 2007; Tenorio et al., 2013). Reduced GLT-1 expression has been associated with a number of neurodegenerative diseases, neurotrauma, and the presentation of neuropathic pain (Higashimori et al., 2013; Piniella et al., 2018).

The close contact between astrocytes and neurons can also influence the function, formation, maturation, and deletion of synapses and dendritic spines (Ventura and Harris, 1999; Loov et al., 2012; Broadhead et al., 2020). The way that astrocytes and neurons interact with each other is largely influenced by Ras-related C3 botulinum toxin substrate 1, also known as Rac1. Rac1 is a small GTPase molecule that rearranges actin filaments, resulting in changes to astrocyte motility and shape. Blocking Rac1 has been shown to prevent the astrocytic movement required for normal tripartite synapse function (Ziegenfuss et al., 2012; Fan et al., 2021).

Our previous work has indicated that Rac1-dependent dendritic spine dysgenesis on spinal cord motor neurons contributes to the development of hyperreflexia after SCI (Bandaru et al., 2015; Benson et al., 2021). In these studies, SCI animals treated with the small molecule Rac1 inhibitor, NSC23766, or with a conditional Rac1KO in α -motor neurons displayed reduced H-reflex hyperexcitability, that is, less spasticity. The Rac1 targeted physiological effects were associated with a reduction in abnormal dendritic spine profiles on α -motor neurons (Bandaru et al., 2015; Benson et al., 2021). Notably, these studies did not investigate the possible role of astrocytic Rac1 on neighboring α -motor neurons and post-SCI hyperreflexia.

To understand the specific contribution of astrocytic Rac1 in the development of spasticity following SCI, in the present study, we generated a selective Rac1KO in astrocytes using a cre-lox system (GFAP-cre/Rac1^{fllox/fllox}) in a mouse model of spasticity. Our results demonstrate for the first time that Rac1 activity in astrocytes is associated with hyperreflexia and spasticity following SCI. These findings highlight the need to consider glial cells as well as neurons while developing treatment regimens to manage post-traumatic spasticity.

Materials and Methods

Animals

Experiments were performed in accordance with the National Institutes of Health *Guidelines for the Care and Use of Laboratory Animals*. All animal protocols were approved by the Yale University/Veterans Affairs Institutional Animal Use Committee. Animals were housed under a 12 h light/dark cycle with food and water provided ad libitum. Eight- to 10-week-old male and female mice (c57/bl6) underwent either Sham or SCI surgery. A total of 56 animals were used between Sham-Rac1^{wt} ($n = 8$), Sham-Rac1KO ($n = 9$), SCI-Rac1^{wt} ($n = 19$), and SCI-Rac1KO ($n = 20$) groups (Fig. 1A). An additional four uninjured animals (WT $n = 2$, astrocytic Rac1KO $n = 2$) were used for tissue culture.

Experimental animals were conditional tdTomato reporter Gt(ROSA)26Sortm9(CAG-tdTomato)Hze/J (Jackson Laboratory, stock #007909) crossed with Rac1^{fllox} (Jackson Laboratory, stock #005550) and GFAP-Cre (Jackson Laboratory, stock #024098; Rac1KO). Control animals were littermates with conditional GFAP-Cre tdTomato expression and WT Rac1 (Rac1^{wt}). The genotype of each animal was confirmed by PCR prior to study inclusion.

Astrocyte cultures

To confirm the Rac1KO, spinal cord astrocytes were isolated from 8-week-old Rac1^{wt} or Rac1KO animals and immunolabeled for Rac1 expression. The isolation and culture of adult spinal cord astrocytes were adaptive from the protocol described by Beaudet et al. (2015). Briefly, the spinal cord was dissected out into a cold neuronal isolation medium (NIM) containing Leibovitz's L-15 medium (Life Technologies, catalog #21083027), 2% B27, 0.5 mM GlutaMAX and 100 U/ml penicillin, and 100 mg/ml streptomycin. Subsequently, the spinal cord was transferred to a digestion medium made up of NIM containing papain (25 U/ml; catalog #LS003126, Worthington Biochemical) and DNase I (2,000 U/ml; catalog #0453628001). We incubated it at room temperature (RT) for 5 min while dissecting the isolated spinal cord into four approximately equal pieces using a scalpel followed up with incubation in a digestion medium at 37°C for 30 min. Following incubation, 3 ml of ice-cold NIM was added and centrifuged at 4°C for 10 min at 280 g. The disassociated cells were washed by removing the supernatant, adding cold NIM, and triturating 3 \times , followed by centrifugation at 4°C for 10 min at 300 g. The pellet containing glial cells was plated and incubated at 37°C in C2C12 cell conditioned Neurobasal A medium (Life Technologies, catalog #12349-015) containing 2% B27, 0.5 mM L-glutamine (Life Technologies, catalog #21051-024), 100 U/ml penicillin, and 100 mg/ml streptomycin, NT3, GDNF, BDNF, and CNTF.

Immunolabelling, image acquisition of cultured astrocytes, and quantification

For immunolabelling of Rac1, astrocyte cultures were fixed with 4% PFA in PBS with 0.1% Triton X-100 for 10 min. Fixed tissue was permeabilized with 0.1% Triton X-100 in PBS for 5 min. Cells were washed three times in PBS and then blocked at RT with gentle shaking for 1 h in 2% bovine serum albumin and 5% normal donkey serum. After blocking, cells were incubated with 1:100 mouse anti-Rac1 (Cytoskeleton, catalog #ARC03) at 4°C overnight. The next day, cells were washed three times with PBS and incubated with donkey anti-mouse 647 (Jackson Laboratory, 711-496-152), at RT for 1 h. Images were captured with the same acquisition settings across groups using an Andor spinning disc confocal microscope (Oxford Instruments) and a 20 \times water immersion Nikon objective. Rac1 immunofluorescence intensity in astrocytes was quantified using the NIH ImageJ software. Both Rac1KO and Rac1^{wt} animals express GFAP-cre-dependent tdTomato. Here, the detection of tdTomato was used as a marker of astrocytes and the presence of active cre-recombinase. In ImageJ, the *particle analysis function* was used to automatically select and outline individual tdTomato expressing astrocytes. We measured the fluorescence intensity of Rac1 immunolabeling in these outlined astrocytes. To account for intracellular autofluorescence, Rac1 fluorescence intensity was normalized to the average intensity of astrocytic nuclei (i.e., no Rac1 present) for each culture. In cases where the average autofluorescence was brighter than Rac1 immunofluorescence, these cells were given a value of zero. Note that *any residual* fluorescence in Rac1KO astrocytes was due to background noise. A total of $n = 238$ (WT $n = 156$, astrocytic Rac1KO $n = 82$) neurons were analyzed from four cultures (WT $n = 2$, astrocytic Rac1KO $n = 2$).

RNA scope fluorescence in situ hybridization

The gene expression of *Gfap* and *Slc1a2* (GLT-1) was analyzed using RNA scope fluorescence in situ hybridization (FISH) technique from Advanced Cell Diagnostics. Briefly, 3 weeks after SCI/Sham surgery, animals were euthanized under ketamine/xylazine anesthesia (100/10 mg/kg, i.p.) and then subjected to intracardial perfusion with ice-cold PBS followed by 4% PFA (0.01 M PBS). The lumbar enlargement spinal cord tissue (L4–L5) was extracted and post-fixed in 4% PFA at 4°C overnight. Tissue sections were cut into 20 μm thickness

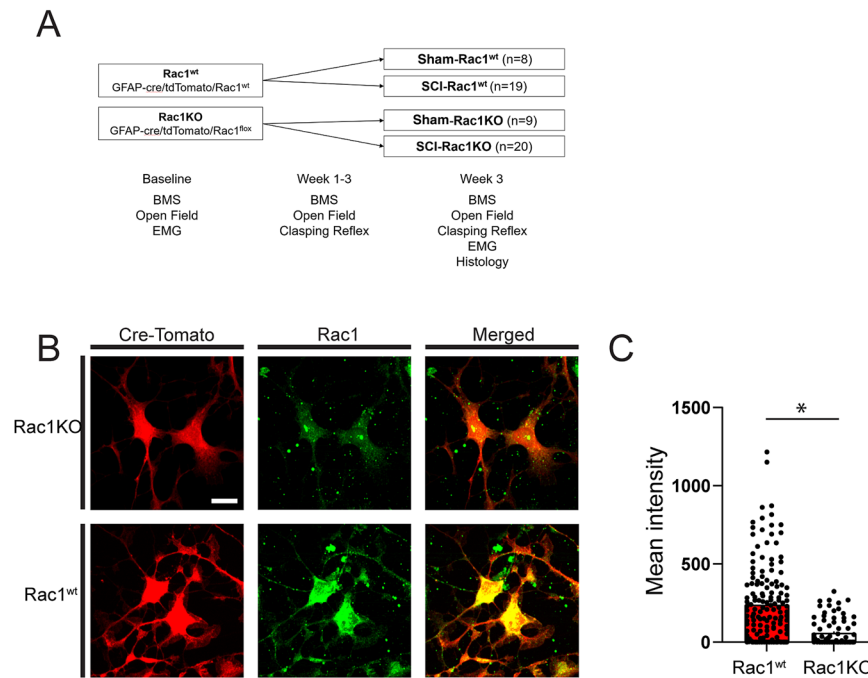


Figure 1. Study design and confirmation of Rac1KO in astrocytes. **A**, Study design and timing of behavioral testing, EMG assessment, and histological analysis. **B**, Immunofluorescent labeling of cultured astrocytes from Rac1KO and Rac1^{wt} animals was used to confirm the absence of Rac1. Rac1 could not be detected in tdTomato (cre-dependent)-positive cells isolated from GFAP-cre/Rac1^{flox/flox} animals. **C**, Quantification of Rac1 immunofluorescence intensity in astrocytes from Rac1KO and Rac1^{wt} animals (**p* < 0.05). Scale bar in **B** = 10 μm and applies to all images.

using a cryostat (Leica Biosystems) and directly mounted on Superfrost Plus slides (Fisher Scientific). The spinal cord tissue sections were pre-treated and hybridized with probes specific to mouse *Gfap* or *Slc1a2* (Advanced Cell Diagnostics) following the manufacturer's protocols in the RNAscope Multiplex Fluorescent V2 Assay kit (Advanced Cell Diagnostics). Fluorophores Opal520, Opal570, and Opal650 were obtained from Akoya Biosciences. Finally, the sections were mounted with ProLong Diamond Antifade Mountant with DAPI (Thermo Fisher Scientific).

Quantification of RNAscope

To quantify the RNAscope results, images of the spinal cord tissue were captured using an Andor BC43 benchtop confocal microscope (Oxford Instruments). Image stacks were obtained at 2,048 × 2,000 pixel resolution using a Nikon 40× 1.3 NA oil immersion objective. The RNA expression, represented by the number of fluorescence puncta, was quantified using the open-source image analysis software QuPath (Bankhead et al., 2017). For detailed instructions on analyzing RNAscope images using QuPath v0.4.3, a technical note is available on the Advanced Cell Diagnostics website. In summary, to create a single-plane image, the image stacks were opened in ImageJ (National Institutes of Health). To minimize overlapping cell nuclei, only a 5 μm range of the total image stack was projected into a single plane. Next, the “cell detection” function in QuPath was used to automatically outline the DAPI-stained cell nuclei. Subsequently, the “subcellular detection” function was utilized to count the number of *Gfap* or *Slc1a2* fluorescence puncta within each segmented nucleus. The expression of *Slc1a2* was then quantified within nuclei expressing more than 10 *Gfap* puncta, that is, astrocytes. The changes in the expression of *Slc1a2* were reported as a percentage of Sham-Rac1^{wt} levels (% control) across the Sham and SCI groups. A total of two tissue sections were analyzed per animal, with the following group sizes: Sham-Rac1^{wt} *n* = 4, Sham-Rac1KO *n* = 4, SCI-Rac1^{wt} *n* = 4, and SCI-Rac1KO *n* = 4.

Spinal cord injury

For SCI, we followed a similar protocol to our previous studies, which has been shown to produce spasticity beginning 3 weeks after SCI (Bandaru et al., 2015; Benson et al., 2021). In brief, mice were anesthetized with

1–3% isoflurane, and the 12th thoracic vertebra (T12) was partially removed to expose the L2 spinal cord surface (Hebel and Stromberg, 1976). A mild severity spinal contusion injury model was performed with the Infinite Horizon impactor (Precision Systems and Instrumentation; Nishi et al., 2007). A metal rod (diameter, 1.3 mm) was applied to the exposed dorsal surface with a 60 kdyn impact force. We measured biomechanical data for actual impact force and spinal cord displacement (μm; Fig. 2*A,B*). For Sham, animals underwent the same procedures, but without SCI. Following surgeries, muscle, fascia, and skin were closed with 6–0 monofilament sutures. Postoperative treatments included twice daily monitoring and postoperative injection of 0.9% saline solution (3.0 ml, s.c.) and Baytril (0.3 ml, 3.5 mg/kg).

Behavioral assays

Basso mouse scale. To validate equivalent injury across SCI animals and overall locomotor ability, blinded investigators monitored animals using the Basso mouse scale (BMS; Basso et al., 2006). The BMS grades locomotor function with 0–9 scores: 0 indicates complete paralysis of the hindlimbs, and 9 indicates normal locomotor ability. Following baseline BMS measurements, animals with SCI were scored weekly, and the average score in each week was compared across groups.

Open field assay. Exploratory behavior was assessed using the open field assay. Animals were placed in an opaque plastic container (width, 29 cm; length, 44 cm; height, 17 cm) in a dimly lit room and video recorded for a 30-min period. The total distance traveled was analyzed using the open-source software ToxTrac (Rodriguez et al., 2018). The ratio of pixel size to centimeter was calibrated for each video compensating for any changes in camera and open field position.

Hindlimb clasp reflex. Hindlimb clasp reflex, a behavior observed in several models of neurological disease and injury (Lalonde and Strazielle, 2011), has been suggested by multiple studies to be an indicator of spasticity (Qiang et al., 2019; Loy et al., 2021). To quantify hindlimb clasp reflex behavior, we adapted previous methods that implement an ordinate scoring system (Cahill et al., 2019; Svensson et al., 2020). In this approach, we suspended SCI animals by their

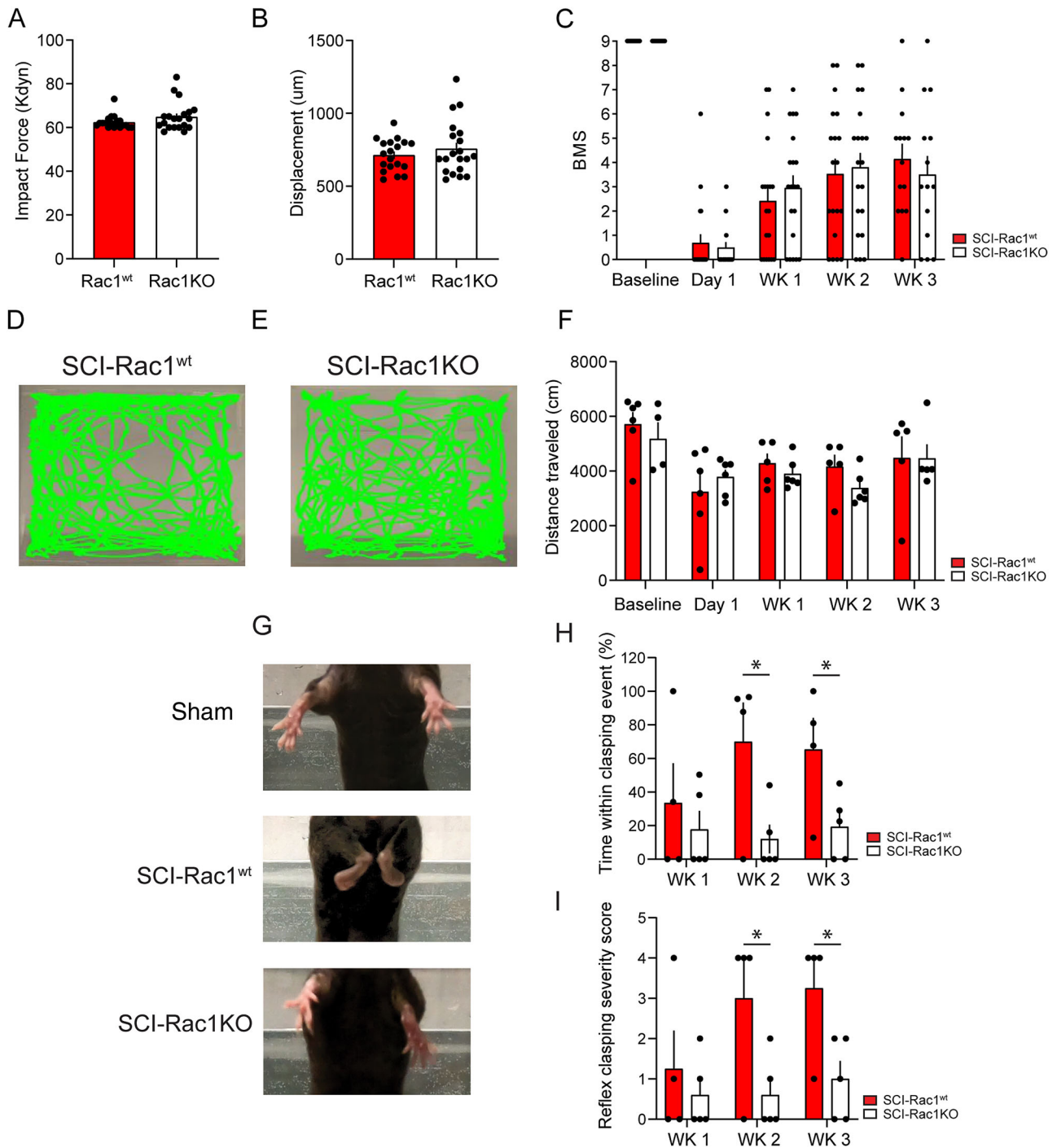


Figure 2. Rac1KO in astrocytes did not alter recovery after SCI. **A, B**, Biomechanical impact data provided by the Infinite Horizon device demonstrates that SCI-Rac1^{wt} and SCI-Rac1KO groups received consistent injuries. **C**, Blinded observers performed BMS testing at baseline and weekly following SCI (Wk1–Wk3). Both SCI-Rac1^{wt} and SCI-Rac1KO groups recovered equally over a 3-week period. **D–E**, Representative images of exploratory behavior in an open field over 30 min. **F**, Rac1KO did not impact activity in the open field after an injury, and animals from SCI-Rac1^{wt} and SCI-Rac1KO groups displayed a reduced distance traveled ($n = 4–6$ per group). **G–I**, SCI-Rac1KO animals displayed less reflex clasp behavior 2–3 weeks post-SCI compared to SCI-Rac1^{wt} ($n = 4–5$ per group). **G**, Representative images showing reflex clasp behavior in SCI-Rac1^{wt}, which was not observed in Sham animals and occurred significantly less in animals with astrocytic Rac1KO. **H**, SCI-Rac1^{wt} animals showed an increased severity of hindlimb clasp 2–3 weeks after SCI as compared to SCI-Rac1KO ($*p < 0.05$). **I**, SCI-Rac1^{wt} spent a greater percentage of time within a clasp event compared to SCI-Rac1KO ($*p < 0.05$). Graphs are mean \pm SEM.

tail for 15 s, and the reflexive positioning of their hindlimbs was quantified. SCI animals were scored on a four-point scale as follows: 0, normal splaying of the hind limbs; 1, clasp of one hindlimb for less than 50% of the observation period; 2, clasp both hindlimbs for less than 50% of the observation period; 3, clasp one hindlimb for more than 50% of the observation period; and 4, clasp both

hindlimbs for more than 50% of the observation period. Additionally, we recorded the time spent in a clasp event as a percentage of the total observation period (15 s). Because Sham animals without SCI, that is, WT and Rac1KO, did not exhibit any clasp reflex behavior, we excluded them appropriately from any comparisons with SCI animals.

EMG H-reflex testing

SCI-Rac1^{wt} and SCI-Rac1KO animals underwent EMG testing under anesthesia. Animals were anesthetized with 100/10 mg/kg intraperitoneal dose of ketamine and xylazine and maintained on ketamine alone (20 mg/kg, i.p.), as we and others published previously (Ho and Waite, 2002; Hosoido et al., 2009). To record EMG data, which included the motor response (M-wave) and the monosynaptic reflex (H-reflex), we used a percutaneous needle preparation (Schieppati, 1987; Thompson et al., 1992; Valero-Cabre et al., 2004; Boulenguez and Vinay, 2009; Lee et al., 2009). This minimally invasive procedure is analogous to methods used to study H-reflex in humans (Schieppati, 1987; Palmieri et al., 2004) and also permitted longitudinal study while maintaining tissue integrity for *postmortem* histology performed at the experimental endpoint.

For stimulation, a pair of Teflon-insulated stainless steel wire electrodes (0.002" diameter; A-M Systems) were threaded through a 32 G syringe needle. The wire ends were bent into sharp barbs. The insulation was removed with heat (exposed tips ~1 mm), and the needle/wire was then transcutaneously inserted with the tip near the tibial nerve. The needle was retracted, and the wire remained in place. A second electrode was inserted similarly ~2 mm away from the first electrode (Ho and Waite, 2002; Hosoido et al., 2009; Bandaru et al., 2015). Stimulating electrode placement was adjusted until square wave stimulating pulses (0.2 ms duration given at a rate of 1 every 3 s) elicited visible motor twitch responses, that is, plantar flexion (Valero-Cabre et al., 2004; Lee et al., 2009). To record EMG data (e.g., plantar reflex), an electrode was inserted into the plantar muscles within the hind paw palmar/ventral surface, proximal to the ankle. A reference electrode was placed subcutaneously in the dorsolateral surface of the hind paw. EMG responses were filtered, amplified, and analyzed offline using Spike 2 software (version 7.08; CED Software). Threshold (T) was defined as the minimum intensity required for an M-wave response ~50% of the time. We used a stimulation intensity that produced consistent M- and H-wave responses (~1.4–1.8T). To measure the rate-dependent depression (RDD) of the H-reflex, we applied a paired-pulse stimulation paradigm: a control pulse and test pulse (0.2 ms square) separated by a range of interpulse intervals (10–2,000 ms). Three trials (10 sweeps/trial) were recorded for each interpulse interval. We quantified the M- and H-wave amplitudes from rectified and averaged waveforms (Boulenguez et al., 2010; Tan et al., 2012). For comparisons, the maximum amplitudes of the H and M response to the test pulse were converted into a percentage of the maximum amplitude response to the control pulse (test/control × 100). M and H waveforms were measured from baseline-to-peak amplitude. To normalize any changes in muscle activity, we calculated the H/M ratio by dividing the %H-reflex by the %M-wave. All H-reflex testing was performed acutely (i.e., recordings lasted <1 h per animal), and we ensured that all animals underwent similar H-reflex testing protocols.

Immunohistochemistry and image analysis

At the experimental endpoint, 3 weeks post-SCI/Sham surgery, animals were euthanized under ketamine/xylazine anesthesia (100/10 mg/kg, i.p.) via intracardial perfusion with ice-cold PBS followed by 4% PFA (0.01 M PBS). Lumbar enlargement spinal cord tissue (L4–L5) was removed and post-fixed in 4% PFA at 4°C overnight. For cryoprotection, we submerged tissue in 30% sucrose for ~48 h. Tissue sections were cut at a thickness of 20 μm using a cryostat (Leica Biosystems) and directly mounted on Superfrost Plus slides (Fisher Scientific). For immunohistochemistry, sections were blocked for 1 h at 25°C in 4% normal donkey serum, 2% bovine serum albumin, 0.1% Triton X-100, and 0.02% 0.01 M PBS. Tissue was incubated in primary antibodies using guinea pig anti-GLT-1 1:500 (Millipore, AB1783). Secondary antibodies included donkey anti-guinea pig 647 (Jackson Laboratory, 711-496-152).

Immunofluorescent Z-stack images were captured with the same acquisition settings across groups using an Andor spinning disc confocal microscope (Oxford Instruments) and a 40× water immersion Nikon objective. Tissue image analysis was conducted by blinded investigators using ImageJ software (National Institutes of Health free download: <http://rsbweb.nih.gov/ij/>). To analyze GLT-1 expression, Z-stack images were compiled into a single plane. Within the ventral horn of the spinal

cord, the mean pixel intensity of threshold-adjusted levels of GLT-1 fluorescence immunoreactivity with the subtracted background was compared as a percent of Sham-Rac1^{wt} levels (% control) across the Sham and SCI groups.

Golgi staining and histology

Tissue was stained by the Golgi method, as described previously (Bandaru et al., 2015; Guo et al., 2018). Briefly, mice were euthanized by decapitation without fixation. Fresh spinal cord tissues from the lumbar enlargement (L4–L5) were rapidly dissected (<5 min), rinsed in distilled water, and processed using a commercial kit (using the manufacturer's instructions; FD NeuroTechnologies). Twenty days later after incubation in the Golgi kit's impregnation solutions, 200-μ-thick coronal sections were cut on a vibratome (Leica VT1200S; Leica Biosystems) and mounted on gelatinized glass slides. Mounted sections were developed, rinsed in distilled water, dehydrated, cleared, and coverslipped using a Permount medium. Golgi-stained sections were visualized with a transmitted light microscope (Nikon Eclipse 80i). Images were captured with an HQ CoolSnap camera (Roper Scientific).

In total, 122 α-motor neurons (Sham-Rac1^{wt} *n* = 30, Sham-Rac1KO *n* = 41, SCI-Rac1^{wt} *n* = 25, SCI-Rac1KO *n* = 26) from 20 animals were traced by a blinded observer using the NeuroLucida software suite (version 9.0; MicroBrightField). The dendritic spine density of each neuron was averaged per animal and compared across groups (Sham-Rac1^{wt} *n* = 4, Sham-Rac1KO *n* = 5, SCI-Rac1^{wt} *n* = 5, SCI-Rac1KO *n* = 6).

To identify α-motor neurons, we followed a screening workflow based on data from our previous study and others (Crockett et al., 1987; Friese et al., 2009; Tan et al., 2012; Bandaru et al., 2015). α-Motor neurons were identified based on their location in ventral horn Rexed lamina IX, with soma diameters >25 μm, and cell body cross-sectional areas >450 μm² (Bandaru et al., 2015). As a refinement step for analysis a priori, we only included α-motor neurons for analysis that had a visible cell body and with greater than one dendritic branch. We analyzed the completed three-dimensional reconstructions of motor neurons for dendritic spine density and distribution. Dendritic spine types (thin spines and mushroom spines) were located and marked on each reconstructed dendritic branch. Classification into only thin and mushroom spines allowed us to use strict rules to classify spine morphology: thin spines had head diameters that were less than or equal to the length of the spine neck, whereas mushroom spines had spine head diameters that were greater than the length of the spine neck. Dendritic spine density was expressed as dendritic spine number per micrometer dendrite length. To determine any changes in the spatial distribution of dendritic spines relative to the cell body, we used Sholl's analysis (Tan et al., 2008). Dendritic spine density within *proximal* (0–40 μm), *medial* (40–80 μm), and *distal* (80–120 μm) regions from the cell body were averaged within each group and compared across groups.

Statistical analysis

All statistical tests were performed at the α-level of significance of 0.05 by two-tailed analyses using parametric or nonparametric tests, as appropriate. Normality assumptions of each data set were determined using a Shapiro–Wilk test. As appropriate, we applied the unpaired *t* test, Mann–Whitney *U* test, or two-way ANOVA in cohort comparisons. Following the detection of statistical differences using two-way ANOVA, pairwise comparisons were analyzed using post hoc Bonferroni tests. Data management, statistical analyses, and graph generation were performed using SigmaPlot 13.0 (Systat), GraphPad Prism 9.5.1, and Microsoft Office Excel. All data are presented as mean ± SEM (graphs and text).

Results

Astrocytic Rac1KO does not impair gross locomotor recovery following SCI

To confirm the absence of Rac1, we cultured adult spinal cord astrocytes and immunolabeled for Rac1 (Fig. 1*B*). Rac1 was absent from tdTomato-positive astrocytes taken from GFAP-crc/Rac1^{flox/flox} (Rac1KO) animals, whereas Rac1 expression

measured as mean fluorescence intensity was readily detected in astrocytes from Rac1^{wt} animals ($t_{(236)} = 6.237$, $p < 0.001$; Rac1^{wt} vs Rac1KO; 237.6 ± 20.18 vs 58.4 ± 9.7 mean intensity; unpaired t test; Fig. 1B,C). Note that prior to inclusion in the study, animal genotype was also determined using PCR to detect the presence or absence of GFAP-cre and Rac1^{fllox} in the genome (data not shown).

To confirm equivalent SCI severity across experimental groups, we analyzed the applied impact force and maximum spinal cord displacement from the Infinite Horizon device (Fig. 2A, B). These metrics predict the amount of tissue sparing in this model and correlate well with locomotor recovery (Scheff et al., 2003). There was no difference in the amount of applied impact force between Rac1^{wt} ($n = 19$) and Rac1KO ($n = 20$) groups ($U = 153.5$, $p = 0.307$; Rac1^{wt} vs Rac1KO; 62.4 ± 0.7 vs 64.9 ± 1.5 kDyn; Mann–Whitney U test; Fig. 2A). In addition, we observed no difference in the maximum spinal cord displacement between groups ($t_{(37)} = 0.898$, $p = 0.375$; Rac1^{wt} vs Rac1KO; 712.8 ± 25.0 vs 757.0 ± 41.6 ; unpaired t test; Fig. 2B).

To determine whether astrocytic Rac1KO influenced locomotor ability, animals underwent weekly BMS open field testing (Basso et al., 2006). Over the course of the study, there was no difference in motor recovery between the Rac1^{wt} and astrocytic Rac1KO groups (Fig. 2C). As expected, 1 day after SCI, animals display hindlimb paralysis with minimal ankle movement ($t_{(37)} = 0.440$, $p = 0.662$; SCI-Rac1^{wt} vs SCI-Rac1KO; 0.7 ± 0.4 vs 0.5 ± 0.2 BMS score, unpaired t test; Fig. 2C). Three weeks post-SCI, both Rac1^{wt} and Rac1KO animals recovered equally ($t_{(26)} = 0.652$, $p = 0.520$; SCI-Rac1^{wt} vs SCI-Rac1KO; 4.1 ± 0.6 vs 3.5 ± 0.8 BMS score, unpaired t test; Fig. 2C).

In addition, we analyzed gross locomotor function and exploratory behavior using the distance traveled in an open field over a 30-min period (Fig. 2D,E). Over the 3 weeks following SCI, both Rac1^{wt} and Rac1KO groups displayed a similar total distance traveled during the 30 min open field test (day 1 post-SCI distance: $t_{(7)} = 0.054$, $p = 0.958$; SCI-Rac1^{wt} vs SCI-Rac1KO, $3,808.5 \pm 445.1$ vs $3,781.5 \pm 270.6$ cm, unpaired t test; week 3 post-SCI distance: $t_{(8)} = 0.015$, $p = 0.988$; SCI-Rac1^{wt} vs SCI-Rac1KO; $4,476.4 \pm 793.9$ vs $4,462.1 \pm 514.9$ cm, unpaired t test; Fig. 2F), which indicates that Rac1KO in astrocytes did not influence locomotor recovery after SCI.

To investigate whether Rac1KO affected non-gross motor-related reflex function, we monitored hindlimb clasp reflex behavior following SCI. Multiple studies have noted abnormal hindlimb clasp reflex, in various models of neurological pathology and trauma (Qiang et al., 2019; Loy et al., 2021), including Huntington's disease, Alzheimer's disease, and Rett syndrome (Lalonde and Strazielle, 2011; Cahill et al., 2019). Animals were monitored weekly for the development and severity of the hindlimb clasp reflex behavior using a four-point severity scale [ordinate scoring system adapted from Cahill et al. (2019)] and recorded the time within a clasp event. Note that hindlimb clasp reflex behavior was absent in both Sham animals with WT Rac1 (Sham) and Sham animals with astrocytic Rac1KO (Sham-Rac1KO) and were not included in the analysis (Fig. 2G–I). At 2 and 3 weeks post-injury, SCI-Rac1^{wt} animals spent a significantly greater amount of time displaying clasp reflex (SCI-Rac1^{wt} vs SCI-Rac1KO: week 2, $t_{(7)} = 2.549$, $p = 0.038$, 70.0 ± 23.4 vs 12.0 ± 8.6 ; week 3, $t_{(7)} = 2.399$, $p = 0.048$, 65.4 ± 18.7 vs 19.4 ± 8.7 time within clasp event; unpaired t test; Fig. 2H). In addition, the SCI-Rac1KO reduced the severity of the clasp reflex at 2 and 3 weeks post-SCI compared to Rac1^{wt} animals (SCI-Rac1^{wt} vs SCI-Rac1KO: week 2, $t_{(7)} = 2.428$,

$p = 0.046$, 3.0 ± 1.0 vs 0.6 ± 0.4 ; week 3, $t_{(7)} = 2.707$, $p = 0.03$, 3.25 ± 0.75 vs 1.0 ± 0.5 reflex clasp severity score, unpaired t test; Fig. 2I).

Astrocytic Rac1KO reduces H-reflex hyperexcitability after SCI

A loss of RDD is indicative of hyperreflexia and spasticity and is observed after SCI in humans and animals (Nielsen et al., 2007). To determine whether Rac1KO from astrocytes could reduce hyperreflexia after SCI, we performed longitudinal EMG recordings to measure evoked M-wave and H-reflex response following percutaneous stimulus of the tibial nerve (Bandaru et al., 2015; Fig. 3A). To measure H-reflex RDD, we used a paired-pulse paradigm, which consisted of a control and test stimulus, separated by interpulse intervals ranging from 50–2,000 ms. RDD was quantified as %H-reflex, where the amplitude response from the test stimulus was compared to the amplitude response of the control stimulus and expressed as a percent (Fig. 3B). Representative EMG traces at baseline and after SCI demonstrate that the stimulation protocol produced quantifiable M-wave and H-reflex responses (Fig. 3A). At baseline, the shorter interpulse intervals (i.e., 50 ms) produce the expected loss of H-wave response in the test pulse (orange line) compared to the control pulse (black line; Fig. 3A).

To determine whether astrocytic Rac1KO alone altered H-reflex excitability, we analyzed EMG recordings prior to injury (baseline). At baseline, we observed a subtle hyperexcitability phenotype H-reflex response of animals with astrocytic Rac1KO. Specifically, baseline-Rac1KO animal displayed an increase in %H-reflex at the shorter 50 ms interpulse interval compared to baseline-Rac1^{wt} ($t_{(32)} = 2.207$, $p = 0.034$; baseline-Rac1^{wt} vs baseline-Rac1KO; 50 ms: 26.0 ± 5.0 vs 41.4 ± 5.0 %H-reflex; unpaired t test; Fig. 3B). The M-wave response is a measure of the direct stimulation of the muscle. There was no difference in %M-wave at baseline between Rac1^{wt} and Rac1KO groups (baseline-Rac1^{wt} vs baseline-Rac1KO; at 50 ms: $t_{(34)} = 0.191$, $p = 0.49$, 81.7 ± 5.5 vs 101.2 ± 13.0 ; at 100 ms: $t_{(37)} = 0.317$, $p = 0.91$, 93.5 ± 4.3 vs 91.4 ± 5.1 ; at 150 ms: $t_{(37)} = 1.221$, $p = 0.230$; 93.8 ± 2.7 vs 100.8 ± 5.1 ; at 300 ms: $t_{(36)} = 1.256$, $p = 0.217$; 98.0 ± 1.0 vs 94.2 ± 2.8 ; at 500 ms: $t_{(37)} = 0.901$, $p = 0.20$; 101.3 ± 1.8 vs 96.1 ± 2.4 ; at 1,000 ms: $t_{(37)} = 0.901$, $p = 0.371$; 99.3 ± 1.8 vs 97.0 ± 1.7 ; at 2,000 ms: $t_{(37)} = 0.337$, $p = 0.737$, 100.0 ± 3.7 vs 98.7 ± 1.0 ; unpaired t test). There was no difference in the H/M ratio between baseline-Rac1^{wt} and baseline-Rac1KO. Both groups displayed a positive correlation between increasing interpulse intervals and H/M ratio, indicative of RDD (linear regression: baseline-Rac1^{wt}, $p < 0.0001$; slope, 0.00028; y -intercept, 0.38; baseline-Rac1KO, $p < 0.0001$; slope, 0.00021; y -intercept, 0.52; Fig. 3D).

To assess the effect of astrocytic Rac1KO on the development of SCI-related hyperreflexia, we tested M-wave and H-wave responses 3 weeks after SCI (Figs. 1A, 3A). In agreement with our previous studies, SCI-Rac1^{wt} animals displayed an exaggerated %H-reflex at 50, 100, and 500 ms interpulse (Fig. 3E), indicating hyperreflexia 3 weeks post-SCI. In contrast, in animals with astrocytic Rac1KO, we detected reduced %H-reflex activity compared to SCI-Rac1^{wt} animals (SCI-Rac1^{wt} vs SCI-Rac1KO; at 50 ms: $t_{(35)} = 3.471$, $p = 0.001$, 70.9 ± 9.3 vs 34.2 ± 5.7 ; at 100 ms: $t_{(36)} = 3.305$, $p = 0.002$, 74.9 ± 7.4 vs 44.9 ± 5.4 ; at 500 ms: $t_{(36)} = 2.228$, $p = 0.032$, 81.1 ± 4.9 vs 63.5 ± 6.1 ; %H-reflex; unpaired t test; Fig. 3E).

We also measured the direct activation of spinal motor neurons, that is, M-wave, and observed no difference in % M-wave at any interpulse interval between, SCI-Rac1^{wt}, and SCI-Rac1KO (SCI-Rac1^{wt} vs Rac1KO; at 50 ms: $t_{(34)} = 1.204$,

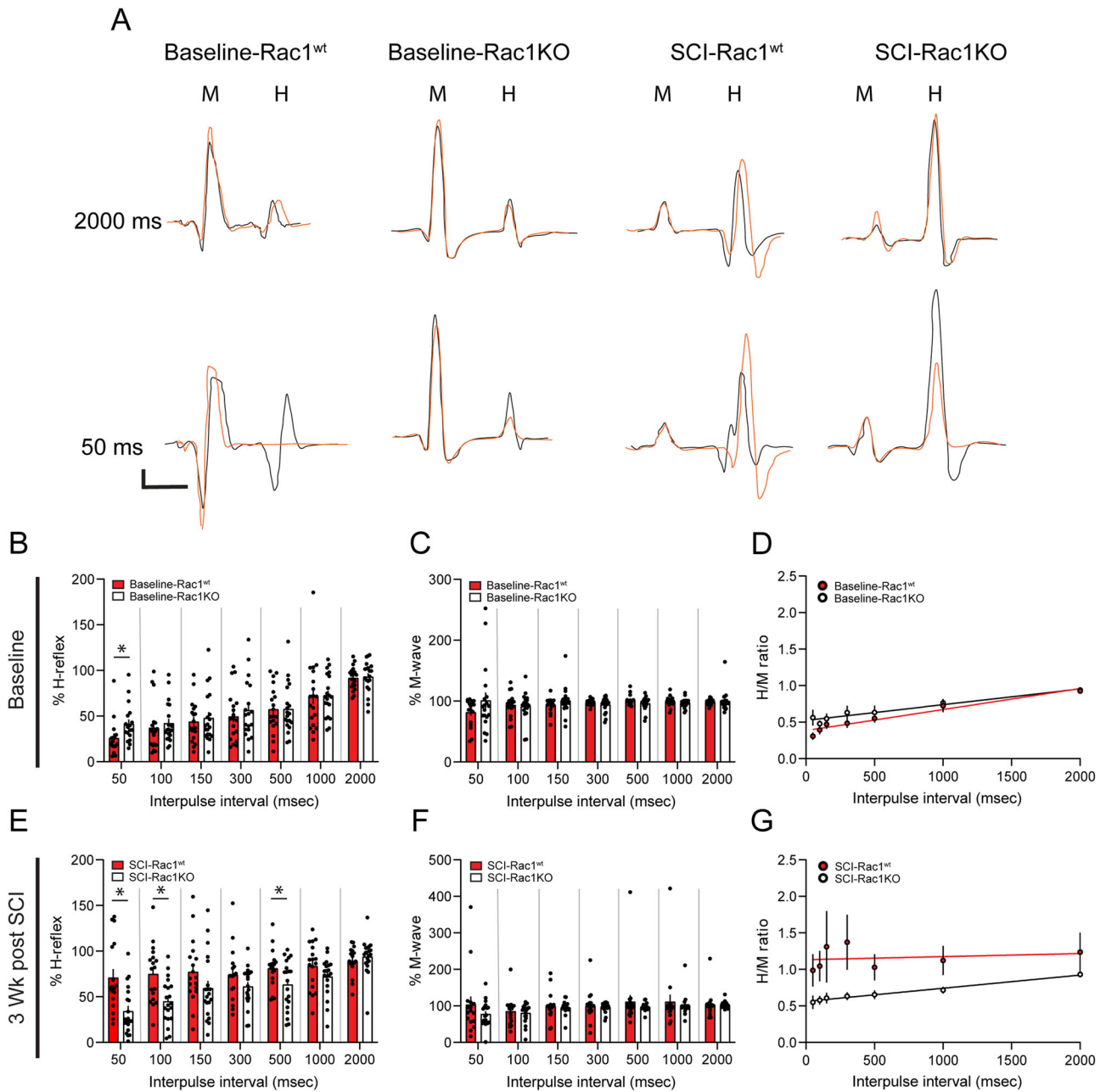


Figure 3. Knockout of Rac1 in astrocytes prevented the development of hyperreflexia after SCI. Representative control (black line) and test (orange line) traces of evoked H-reflex and M-wave responses in **A** baseline-Rac1^{wt}, baseline-Rac1KO, SCI-Rac1^{wt}, and SCI-Rac1KO. The control and test pulses were separated with a range of interpulse latencies between 50 and 2,000 ms. **B–D**, Comparison of %H-reflex, %M-wave, and H/M ratio between Rac1^{wt} and Rac1KO at baseline, prior to receiving spinal cord injury. **B**, As expected at baseline in Rac1^{wt} animals, at shorter interpulse intervals (e.g., 50 ms), the amplitude of the test pulse H-reflex was reduced. **B**, At baseline, Rac1KO animals displayed a slight increase in the %H-reflex at the 50 ms interval compared to Rac1^{wt} animals (**p* < 0.05). **C**, There was no difference in %M-wave between Rac1^{wt} and Rac1KO groups at baseline. **D**, In addition, there was no difference in the H/M ratio between Rac1^{wt} and Rac1KO. Rac1^{wt} and Rac1KO animals had similar H/M ratios across all interpulse intervals, demonstrating RDD in both groups. **E–G**, Comparison of %H-reflex, %M-wave, and H/M ratio between Rac1^{wt} and Rac1KO 3-weeks post-SCI. **E**, After SCI, Rac1^{wt} animals have an exaggerated %H-reflex at 50 and 100 ms interpulse intervals, indicative of hyperreflexia. Rac1KO in astrocytes restored %H-reflex to levels similar to baseline (**p* < 0.05). **F**, There was no difference in %M-wave amplitude between Rac1^{wt}, Rac1KO, and baseline. **G**, SCI increased the H/M ratio as demonstrated as a flat linear trend line compared to a closer-to-normal H/M ratio, with a steeper linear trend line in Rac1KO and baseline groups. Note that in **Figure 3G,K**, the interpulse interval is graphed as a linear scale, to reflect the linear regression analysis (**p* < 0.05). Scale bars in **A–D** = 2 ms (x-axis) and 0.1 spike volts (y-axis), *n* = 19–20 per group, and graphs are mean ± SEM.

p = 0.237, 103.6 ± 22.0 vs 77.9 ± 7.7; at 100 ms: *t*₍₃₆₎ = 0.472, *p* = 0.639, 85.4 ± 8.8 vs 80.5 ± 6.0; at 150 ms: *t*₍₃₆₎ = 0.410, *p* = 0.687, 99.3 ± 8.7 vs 95.6 ± 3.9; at 300 ms: *t*₍₃₆₎ = 0.441, *p* = 0.662, 100.2 ± 9.4 vs 96.1 ± 2.9; at 500 ms: *t*₍₃₆₎ = 0.832, *p* = 0.411, 111.2 ± 18.1 vs 96.9 ± 2.3; at 1,000 ms: *t*₍₃₆₎ = 0.531, *p* = 0.598, 111.6 ± 18.9 vs 101.5 ± 6.3; at 2,000 ms: *t*₍₃₆₎ = 0.222, *p* = 0.825, 103.6 ± 8.1 vs 101.8 ± 2.0; %M-wave, unpaired *t* test; **Fig. 3F**).

The H/M ratio also demonstrated a significant loss of RDD in SCI-Rac1^{wt} animals. A linear regression analysis of the H/M ratio in SCI-Rac1^{wt} revealed no correlation between increasing interpulse intervals and H/M ratio, an indication of RDD loss and hyperreflexia (linear regression: *p* = 0.671, *y* = 1.132 + 0.000004*x*; **Fig. 3G**). In contrast, SCI animals with astrocytic Rac1KO displayed a positive correlation between interpulse interval

and H/M, indicating the presence of RDD, that is, near-normal H-reflex response (linear regression: $p < 0.001$, $y = 0.56 + 0.0002x$; Fig. 3G).

Astrocytic Rac1KO reduces α -motor neuron dendritic spine density after SCI

SCI-induced hyperreflexia is associated with dendritic spine dysgenesis on α -motor neurons, which form part of the monosynaptic reflex loop and drive muscle tissue contraction (Bandaru et al., 2015; Benson et al., 2021). As shown previously, an increase in dendritic spine density is associated with neuronal hyperexcitability after SCI (Tan et al., 2009). To determine whether astrocytic Rac1KO altered the profile of dendritic spines after SCI, we analyzed spinal cord motor neurons using Golgi staining techniques. We identified α -motor neurons based on previously described morphological criteria, which include the soma size and location in lamina IX of the spinal cord ventral horn (Fig. 4A; Crockett et al., 1987). Neurons were reconstructed using NeuroLucida software and dendritic spines were categorized into thin or mushroom-shaped (Fig. 4B). Thin-shaped spines are indicative of immature, less stable synaptic structures, whereas mushroom-shaped spines are considered mature structures with more durable synaptic efficacy (Halpain et al., 2005; Bosch and Hayashi, 2012; Benson et al., 2020). The physiological impact of thin- and mushroom-shaped spines on bioelectrical transduction and neuronal excitability has been well studied (Yuste et al., 2000; Tan et al., 2009; Stratton and Khanna, 2020). To determine the effect of astrocytic Rac1KO on dendritic spines, a morphological correlate of spinal reflex function (Bandaru et al., 2015; Patwa et al., 2019; Benson et al., 2021), we analyzed the density of total-, thin-, and mushroom-shaped dendritic spines on α -motor neurons of Sham, Sham-Rac1KO, SCI-Rac1^{wt}, and SCI-Rac1KO animals (Fig. 5).

Specifically, we compared Golgi-stained motor neurons from Sham animals with astrocytic Rac1KO (Sham-Rac1KO) to Sham animals with WT Rac1 (Sham). We observed a significant increase in the density of total- and thin-shaped spines on α -motor neurons from Sham-Rac1KO animals as compared to Sham WT (Sham vs Sham-Rac1KO; *total spines*: $t_{(16)} = 2.742$, $p = 0.015$; 0.10 ± 0.01 vs 0.18 ± 0.03 total spines/ μm ; *thin spines*:

$t_{(16)} = 3.13$, $p = 0.007$, 0.08 ± 0.02 vs 0.16 ± 0.03 thin spines/ μm ; two-way ANOVA with Bonferroni post hoc test; Fig. 5A,B). Sham-Rac1KO had no effect on the density of mushroom-shaped spines (Sham vs Sham-Rac1KO; *mushroom spines*: $t_{(16)} = 0.001$, $p = 0.998$, 0.017 ± 0.003 vs 0.017 ± 0.004 mushroom spines/ μm ; two-way ANOVA with Bonferroni post hoc test; Fig. 5C). Importantly, this observation agrees with studies that found that astrocytic Rac1KO selectively increases thin-shaped dendritic protrusions on hippocampal neurons (Nishida and Okabe, 2007).

To investigate changes in the distribution of dendritic spines along neuronal branches, we used a modified Sholl's analysis to compare dendritic spine densities within three distinct radii from the soma: *proximal* (0–40 μm), *medial* (40–80 μm), and *distal* (80–120 μm ; Fig. 5D–F). Compared to Sham, astrocytic Rac1KO increased the total density of spines within the medial region and distal regions (Sham vs Sham-Rac1KO; *medial*: $t_{(16)} = 2.683$, $p = 0.016$; 0.10 ± 0.02 vs 0.22 ± 0.04 total spines/ μm ; *distal*: $t_{(16)} = 2.334$, $p = 0.033$; 0.1 ± 0.02 vs 0.19 ± 0.03 total spines/ μm ; two-way ANOVA with a Bonferroni post hoc test; Fig. 5D). When compared to Rac1^{wt}, the increase in thin spine density observed with astrocytic Rac1KO was localized to the medial and distal region (Sham vs Sham-Rac1KO, *medial*: $t_{(16)} = 2.842$, $p = 0.012$; 0.09 ± 0.02 vs 0.2 ± 0.04 thin spines/ μm ; *distal*: $t_{(16)} = 2.696$, $p = 0.016$, 0.08 ± 0.02 vs 0.17 ± 0.03 thin spines/ μm ; two-way ANOVA with Bonferroni post hoc test; Fig. 5E). Astrocytic Rac1KO did not affect the distribution of mushroom-shaped spines when compared to Rac1^{wt} (Sham vs Sham-Rac1KO, *proximal*: $t_{(16)} = 0.589$, $p = 0.564$; 0.017 ± 0.004 vs 0.011 ± 0.002 mushroom spines/ μm ; *medial*: $t_{(16)} = 0.181$, $p = 0.859$; 0.016 ± 0.002 vs 0.018 ± 0.005 mushroom spines/ μm ; *distal*: $t_{(16)} = 0.248$, $p = 0.807$; 0.017 ± 0.004 vs 0.012 ± 0.004 mushroom spines/ μm ; two-way ANOVA with Bonferroni post hoc test; Fig. 5F).

Moreover, as expected with our previous studies (Bandaru et al., 2015; Benson et al., 2021), SCI increased total- and mushroom-shaped spine density on α -motor neurons compared to Sham (Sham vs SCI-Rac1^{wt}; *total spines*: $t_{(16)} = 2.847$, $p = 0.012$, 0.10 ± 0.01 vs 0.18 ± 0.02 total spines/ μm ; *mushroom spines*: $t_{(16)} = 3.130$, $p = 0.001$, 0.017 ± 0.003 vs 0.052 ± 0.008 mushroom spines/ μm ; two-way ANOVA with Bonferroni post hoc test; Fig. 5A,C). SCI animals with astrocytic Rac1KO had a total spine density that was not statistically different from Sham (Sham vs SCI-Rac1KO; $t_{(16)} = 1.322$, $p = 0.205$; 0.10 ± 0.01 vs 0.14 ± 0.02 total spines/ μm ; two-way ANOVA with Bonferroni post hoc test; Fig. 5A). The reduction in total spine density observed in SCI-Rac1KO animals appeared to be driven by the significant decrease in the number of thin spines (SCI-Rac1^{wt} vs SCI-Rac1KO; $t_{(16)} = 2.208$, $p = 0.042$; 0.13 ± 0.02 vs 0.08 ± 0.01 thin spines/ μm ; Sham-Rac1KO vs SCI-Rac1KO; $t_{(16)} = 3.537$, $p = 0.003$, 0.16 ± 0.03 vs 0.08 ± 0.01 thin spines/ μm , two-way ANOVA with Bonferroni post hoc test; Fig. 5B). SCI-Rac1KO animals had an elevated density of mushroom-shaped spine compared to both Sham and Sham-Rac1KO (Sham vs SCI-Rac1KO; *mushroom spines*: $t_{(16)} = 3.770$, $p = 0.002$, 0.017 ± 0.003 vs 0.057 ± 0.01 ; Sham-Rac1KO vs SCI-Rac1KO; *mushroom spines*: $t_{(16)} = 4.017$, $p = 0.001$, 0.017 ± 0.004 vs 0.057 ± 0.01 ; two-way ANOVA with Bonferroni post hoc test; Fig. 5C).

The spatial distribution of dendritic spines along the dendritic branches has a weighted preferential effect on postsynaptic neuronal excitability—for example, excitatory synapses on dendritic spines located closer to the cell body are more likely to generate an action potential. To investigate changes in the distribution of

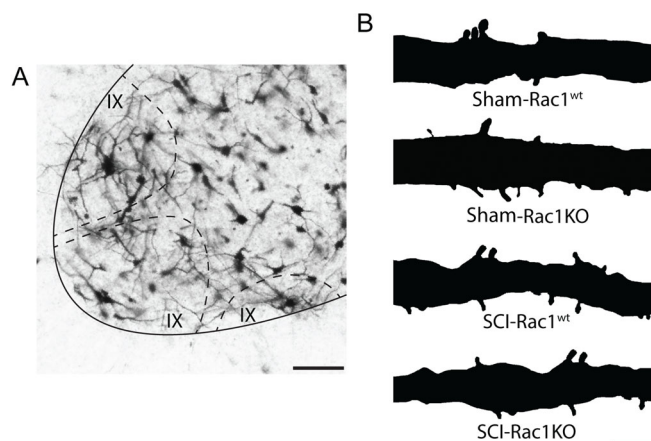


Figure 4. Golgi-stained dendritic spines on spinal motor neurons from Sham-Rac1^{wt}, Sham-Rac1KO, SCI-Rac1^{wt}, and SCI-Rac1KO. **A**, Golgi staining of the spinal cord labels α -motor neuron located in Rexed lamina IX (dashed line). **B**, A reconstructed segment of Golgi-stained motor neuron dendritic branch showing dendritic spines from Sham-Rac1^{wt}, Sham-Rac1KO, SCI-Rac1^{wt}, and SCI in astrocytic Rac1KO. Scale bars in **A** = 50 μm and **B** = 10 μm .

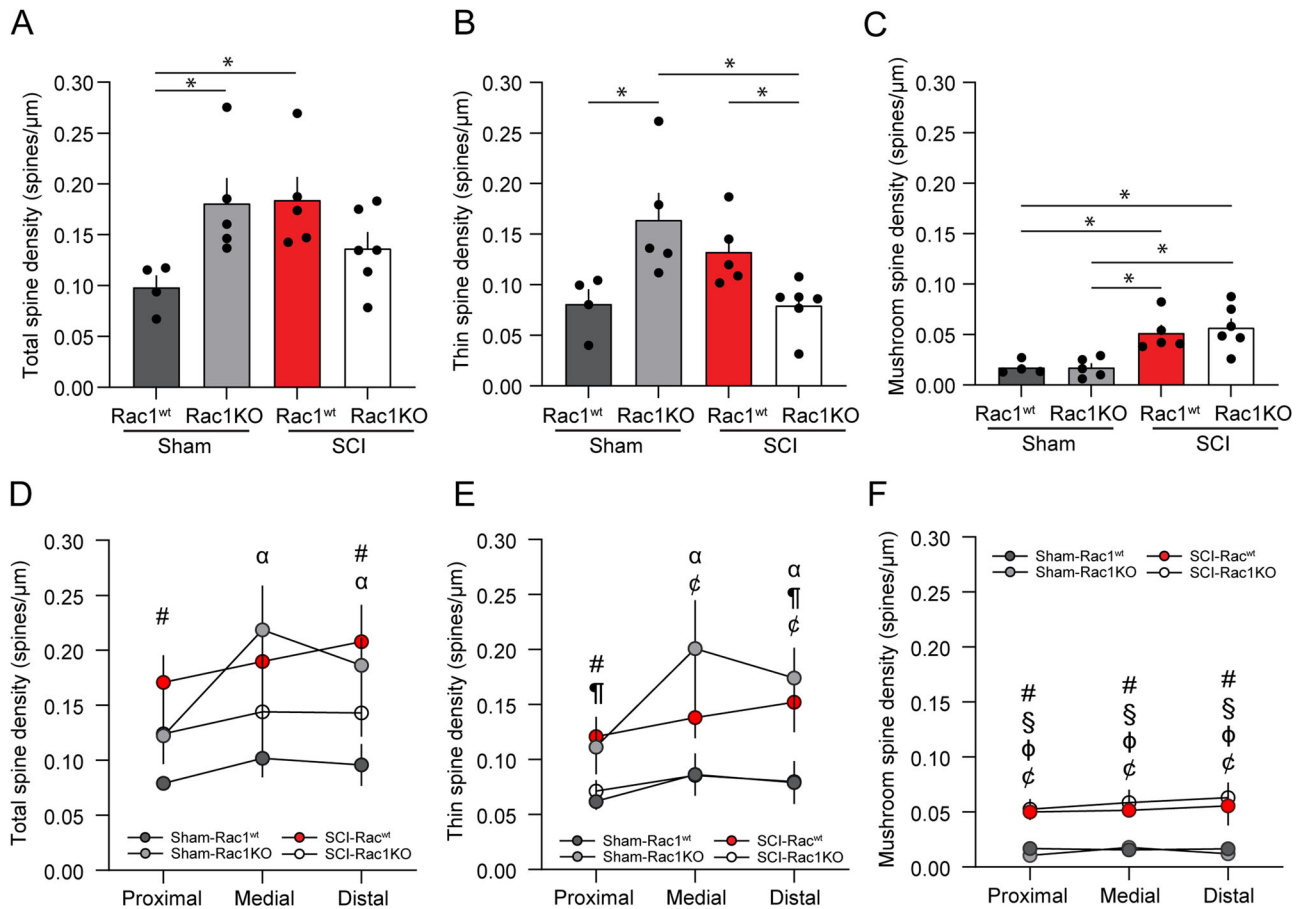


Figure 5. Following SCI, Rac1KO in astrocytes reduces thin, but not mushroom, spine density. Analysis of dendritic spine profiles reveals differences in **A–C** spine density and **D–F** distribution along the dendrite. **A**, Total spine density, which encompasses all spine types, was increased in SCI-Rac1^{wt} compared to Sham-Rac1^{wt} ($*p < 0.05$). Total spine density was elevated in Sham-Rac1KO compared to Sham-Rac1^{wt} ($*p < 0.05$). **B**, Sham-Rac1KO displayed significantly higher thin spine density compared to Sham-Rac1^{wt} ($*p < 0.05$). Thin spine density on spinal motor neurons was lower in SCI-Rac1KO animals compared to SCI-Rac1^{wt} ($*p < 0.05$). SCI-Rac1KO animals displayed less thin density compared to Sham-Rac1KO ($*p < 0.05$). **C**, There was no difference in the density of mushroom-shaped spine between Sham-Rac1^{wt} and Sham-Rac1KO. Both SCI-Rac1^{wt} and SCI-Rac1KO groups showed significantly higher mushroom spine density compared to Sham and Sham-Rac1KO ($*p < 0.05$). However, SCI-Rac1KO was not different from SCI-Rac1^{wt}. Analysis of (**D**) total, (**E**) thin, and (**F**) mushroom spine density within the proximal (0–40 μm), medial (40–80 μm), and distal (80–120 μm) regions from the cell body. **D**, SCI increased the total spine density in the proximal region compared to Sham-Rac1^{wt} ($*p < 0.05$, SCI-Rac1^{wt} vs Sham-Rac1^{wt}). Sham-Rac1KO displayed increased total spine density in the medial and distal region compared to Sham-Rac1^{wt} ($*p < 0.05$, Sham-Rac1^{wt} vs Sham-Rac1KO). **E**, SCI increased thin spine density in the proximal region compared to Sham-Rac1^{wt} ($*p < 0.05$, SCI-Rac1^{wt} vs Sham-Rac1^{wt}). Rac1KO reduced thin spine density in the proximal to the cell body compared to SCI-Rac1^{wt} ($*p < 0.05$, SCI-Rac1^{wt} vs SCI-Rac1KO). Sham-Rac1KO increased thin spine density in the medial and distal region compared to Sham-Rac1^{wt} ($*p < 0.05$, Sham-Rac1^{wt} vs Sham-Rac1KO). SCI-Rac1KO animals had a lower thin spine density compared to Sham-Rac1KO within the medial and distal regions ($*p < 0.05$, Sham-Rac1KO vs SCI-Rac1KO). **F**, SCI led to increased mushroom spine density in all regions in both Rac1^{wt} and Rac1KO groups compared to both Sham groups ($*p < 0.05$, SCI-Rac1^{wt} vs Sham-Rac1^{wt}; $*p < 0.05$, SCI-Rac1KO vs Sham-Rac1^{wt}; $*p < 0.05$, SCI-Rac1^{wt} vs Sham-Rac1KO; $*p < 0.05$, Sham-Rac1KO vs SCI-Rac1KO). $n = 4–6$ animals per group, and graphs are mean \pm SEM.

dendritic spines along neuronal branches, we used a modified Sholl's analysis to compare spine densities within three distinct radii from the soma: *proximal* (0–40 μm), *medial* (40–80 μm), and *distal* (80–120 μm; Fig. 5D–F). Compared to Sham, SCI-Rac1^{wt} elevated the total spine density within the proximal and distal regions (Sham vs SCI-Rac1^{wt}; *proximal*: $t_{(16)} = 3.011$, $p = 0.008$, 0.080 ± 0.004 vs 0.17 ± 0.03 total spines/μm; *distal*: $t_{(16)} = 2.891$, $p = 0.01$; 0.10 ± 0.02 vs 0.21 ± 0.03 total spines/μm; two-way ANOVA with Bonferroni post hoc test; Fig. 5D). The reduction in thin-shaped spine density observed in SCI-Rac1KO animals was localized to the proximal and distal region compared to SCI-Rac1^{wt} (SCI-Rac1^{wt} vs SCI-Rac1KO; *proximal*: $t_{(16)} = 2.162$, $p = 0.046$, 0.15 ± 0.03 vs 0.08 ± 0.02 ; *distal*: $t_{(16)} = 2.273$, $p = 0.037$, 0.15 ± 0.03 vs 0.08 ± 0.02 thin spines/μm; two-way ANOVA with Bonferroni post hoc test; Fig. 5E). SCI in Rac1KO led to a decrease in thin-shaped spine density when compared to Sham-Rac1KO within the medial and distal regions (Sham-Rac1KO vs SCI-Rac1KO; *medial*: $t_{(16)} = 3.170$, $p = 0.006$,

0.20 ± 0.05 vs 0.09 ± 0.02 thin spines/μm; *distal*: $t_{(16)} = 2.963$, $p = 0.009$, 0.17 ± 0.03 vs 0.08 ± 0.02 thin spines/μm; two-way ANOVA with Bonferroni post hoc test; Fig. 5E). Both SCI groups, SCI-Rac1^{wt} and SCI-Rac1KO, produced an increase in mushroom-shaped spine density in all three regions as compared with Sham (*proximal*: Sham vs SCI-Rac1^{wt}; $t_{(16)} = 3.167$, $p = 0.006$, 0.017 ± 0.004 vs 0.050 ± 0.007 ; Sham vs SCI-Rac1KO; $t_{(16)} = 3.557$, $p = 0.003$, 0.017 ± 0.004 vs 0.053 ± 0.009 mushroom spines/μm; *medial*: Sham vs SCI-Rac1^{wt}; $t_{(16)} = 2.862$, $p = 0.011$, 0.016 ± 0.002 vs 0.052 ± 0.006 ; Sham vs SCI-Rac1KO; $t_{(16)} = 3.546$, $p = 0.003$, 0.016 ± 0.002 vs 0.059 ± 0.012 mushroom spines/μm; *distal*: Sham vs SCI-Rac1^{wt}; $t_{(16)} = 2.787$, $p = 0.013$, 0.017 ± 0.004 vs 0.052 ± 0.006 ; Sham vs SCI-Rac1KO; $t_{(16)} = 3.472$, $p = 0.003$, 0.017 ± 0.004 vs 0.059 ± 0.012 mushroom spines/μm; two-way ANOVA with Bonferroni post hoc test; Fig. 5F). Compared to Sham-Rac1KO, SCI-Rac1KO animals displayed an increase in mushroom spine density across the length of the dendrite (Sham-Rac1KO vs SCI-Rac1KO; *proximal*: $t_{(16)} =$

4.444, $p < 0.001$, 0.011 ± 0.002 vs 0.053 ± 0.009 ; medial: $t_{(16)} = 3.580$, $p = 0.003$, 0.018 ± 0.005 vs 0.059 ± 0.012 ; distal: $t_{(16)} = 4.109$, $p < 0.001$, 0.012 ± 0.004 vs 0.063 ± 0.014 mushroom spines/ μm ; two-way ANOVA with Bonferroni post hoc test (Fig. 5F).

Reduced GLT-1 expression in the spinal cord ventral horn of astrocytic Rac1KO animals

A key function of the astrocytes within the CNS is glutamate transport and recycling, for example, neurotransmitter clearance (Danbolt, 2001; Andersen et al., 2021). After SCI, dysregulation of glutamate signaling can adversely alter neuronal excitability (Hefferan et al., 2007; Andersen et al., 2021). To determine whether Rac1KO in astrocytes could potentially influence glutamate homeostasis in the spinal cord reflex circuit, we measured the levels of the astrocytic glutamate transporter, GLT-1 (Fig. 6A). GLT-1 is expressed in astrocytes and mediates the reuptake of extracellular glutamate from the synaptic cleft (Perego et al., 2000). To analyze the relative change in GLT-1 expression, we compared the levels of immunofluorescence intensity as a percent of Sham-Rac1^{wt} control. Comparing Sham and Sham-Rac1KO indicated that astrocytic Rac1KO did not alter the expression of the GLT-1 in uninjured animals ($t_{(7)} = 1.447$, $p = 0.174$, Sham vs Sham-Rac1KO 100.0 ± 10.0 vs $84.3 \pm 6.1\%$ control; $n = 4$ animals per group, two-way ANOVA with Bonferroni post hoc test; Fig. 6B).

A two-way ANOVA revealed that SCI led to an overall increase in GLT-1 expression and that there was a significant interaction between genotype and SCI [SCI vs Sham: $F_{(1,12)} = 33.2$, $p < 0.001$; genotype (Rac1^{wt}/Rac1KO) vs SCI: $F_{(1,12)} = 7.6$, $p = 0.018$; two-way ANOVA; Fig. 6B]. Specifically, pairwise comparisons demonstrated an increase in GLT-1 expression in SCI-Rac1^{wt} animals as compared with Sham-Rac1KO ($t_{(7)} = 3.575$, $p = 0.023$, Sham-Rac1KO vs SCI-Rac1^{wt} 84.3 ± 6.1 vs $123.0 \pm 8.5\%$ control; $n = 4$ animals per group, two-way ANOVA with Bonferroni post hoc test). Animals with astrocytic Rac1KO had the greatest expression of GLT-1 immunofluorescence intensity in the ventral spinal cord as compared with SCI-Rac1^{wt}, Sham, and Sham-Rac1KO (Sham vs Sham-Rac1KO: $t_{(7)} = 4.568$, $p = 0.004$, 100.0 ± 10.0 vs $149.5 \pm 4.9\%$ control; $t_{(7)} = 6.014$, $p < 0.001$; Sham-Rac1KO vs SCI-Rac1KO 84.3 ± 6.1 vs $149.5 \pm 4.9\%$ control; $p = 0.031$; SCI-Rac1^{wt} vs SCI-Rac1KO: 123.0 ± 8.5 vs $149.5 \pm 4.9\%$ control; $n = 4$ animals per group two-way ANOVA with Bonferroni post hoc test; Fig. 6B). This finding suggests a Rac1-dependent role for GLT-1 expression in astrocytes within the spinal cord ventral horn.

To further investigate the effect of Rac1KO on GLT-1 after SCI, we assayed levels of GLT-1 gene expression (*Slc1a2*) in *Gfap*+ nuclei (i.e., astrocytes) within the ventral horn of the spinal cord with and without injury (Fig. 6C). We utilized RNAscope to fluorescently label *Slc1a2* and *Gfap* mRNA, which allowed us to specifically investigate the levels of GLT-1 gene expression within individual astrocytes across animals with and without SCI. Contrary to our investigation of GLT-1 using immunofluorescence labeling, a two-way ANOVA revealed that injury and genotype had a significant effect on *Slc1a2* expression (SCI vs Sham: $F_{(1,12)} = 141.6$, $p < 0.001$, Rac1^{wt} vs Rac1KO: $F_{(1,12)} = 9.564$, $p = 0.009$; $n = 4$ animals per group, two-way ANOVA; Fig. 6D). Pairwise comparisons revealed that SCI led to a decrease in the expression *Slc1a2* in both Rac1^{wt} and Rac1KO groups (Sham-Rac1^{wt} vs SCI-Rac1^{wt}: $q_{(12)} = 13.25$, $p < 0.001$, 100 ± 6.1 vs 35.4 ± 1.9 ; Sham-Rac1^{wt} vs SCI-Rac1KO: $q_{(12)} = 8.808$, $p = 0.002$, 100 ± 6.1 vs 57.0 ± 5.4 ; Sham-Rac1KO vs

SCI-Rac1^{wt}: $q_{(12)} = 14.99$, $p < 0.001$; 108.5 ± 4.9 vs 35.4 ± 1.9 ; Sham-Rac1KO vs SCI-Rac1KO: $q_{(12)} = 10.55$, $p < 0.001$, 108.5 ± 4.9 vs $57.0 \pm 5.4\%$ control; two-way ANOVA with Tukey's post hoc test; Fig. 6D). Despite the SCI-related reduction in *Slc1a2*, SCI animals with Rac1KO had a greater astrocytic *Slc1a2* mRNA expression compared to SCI-Rac1^{wt} (SCI-Rac1^{wt} vs SCI-Rac1KO: $q_{(12)} = 4.440$, $p = 0.037$, 35.4 ± 1.9 vs $57.0 \pm 5.4\%$ control; two-way ANOVA with Tukey's post hoc test; Fig. 6D).

To examine whether SCI led to a change in the number of astrocytes within the ventral horn of the spinal cord, we compared the number of *Gfap*+nuclei normalized for the total number of cells within the analyzed area. As expected, this analysis revealed that SCI led to an increased number of astrocytes within the ventral horn of the spinal cord (SCI vs Sham: $F_{(1, 12)} = 19.6$, $p = 0.001$; $n = 4$ animals per group; two-way ANOVA; Fig. 6E). Comparing the groups indicated that the number of *Gfap*+ nuclei in SCI-Rac1^{wt} was greater than that in both Sham-Rac1^{wt} and Sham-Rac1KO; however, there was no difference compared to SCI-Rac1KO (Sham-Rac1^{wt} vs SCI-Rac1^{wt}: $q_{(12)} = 4.912$, $p = 0.02$, 100 ± 41.5 vs 330.1 ± 69.3 ; Sham-Rac1KO vs, SCI-Rac1^{wt}: $q_{(12)} = 5.980$, $p = 0.006$, 28.0 ± 12.8 vs 330.1 ± 69.3 ; SCI-Rac1^{wt} vs SCI-Rac1KO: $q_{(12)} = 2.037$, $p = 0.500$, 330.1 ± 69.3 vs $234.7 \pm 45.8\%$ control; two-way ANOVA with Tukey's post hoc test; Fig. 6E). Thus, despite that there is a decrease in the expression of astrocytic *Slc1a2* mRNA, there is an overall increase in astrocyte number after SCI, which may account for the increase in GLT-1 protein detected using immunolabelling.

Discussion

Astrocyte activity can directly influence neuronal circuit function after CNS trauma and contribute to chronic hyperexcitability disorders, including central sensitization and hyperreflexia (Hefferan et al., 2007; Ji et al., 2019; Verhoog et al., 2020). As one part of the tripartite synaptic complex, astrocytes have a crucial role in regulating neuronal excitability through glutamate homeostasis and modulating synaptic plasticity. Rac1 activity governs part of these cellular functions through its action on cell motility, ion channel/receptor trafficking, synaptic plasticity, and dendritic spine reorganization (Nishida and Okabe, 2007; Higashimori et al., 2013; Zeug et al., 2018). Injury-induced astrocyte reactivity along with Rac1 could contribute to pathological synaptic transmission and potentiate basal excitability within spinal cord circuits.

Our present study investigated the specific contribution of astrocytic Rac1 in the development of hyperreflexia associated with spasticity following SCI. To investigate the relationship between Rac1 in astrocytes and hyperreflexia, we performed a mild-SCI in GFAP-cre/Rac1^{fllox/fllox} animals (i.e., astrocyte Rac1KO) and assessed for hyperreflexia 3 weeks after injury. As expected from our previous work, 3 weeks after contusion SCI, we observed an abnormal increase in H-reflex response and the loss of RDD, that is, hyperreflexia (Bandaru et al., 2015; Benson et al., 2021). Animals with astrocytic Rac1KO retained RDD following SCI—exhibiting less hyperreflexia—as compared with injured Rac1^{wt} animals.

To support our electrophysiological findings and further investigate the effect of astrocytic Rac1KO on motor reflex function, we tested SCI animals for hindlimb clasp reflex behavior. Currently, there are no firmly established behavioral assays for detecting spasticity in rodents following SCI (Wieters et al., 2021). Although studies in rat models of SCI have suggested that spasticity may be detectable in an open swimming test

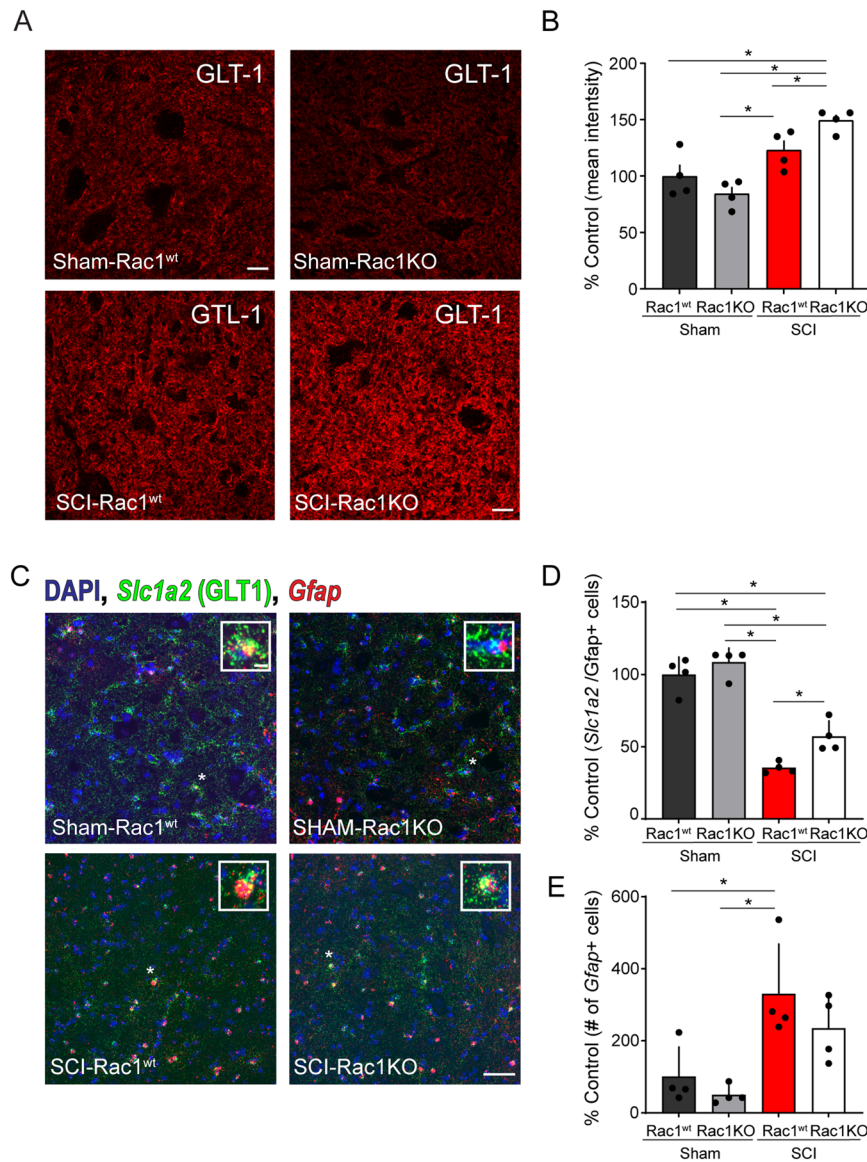


Figure 6. Rac1KO alters the expression of the glutamate transporter GLT-1 in the ventral spinal cord gray matter. Antibody labeling for GLT-1 (**A**) in the ventral horn of the spinal cord in Sham-Rac1^{wt}, Sham-Rac1KO, SCI-Rac1^{wt}, and SCI-Rac1KO. **B**, The expression of GLT-1 (astrocytic glutamate transporter) as a percentage of control (Sham-Rac1^{wt}) levels. The expression of GLT-1 was higher in SCI-Rac1KO compared to both SCI-Rac1^{wt}, Sham-Rac1^{wt}, and Sham-Rac1KO ($*p < 0.05$). There was no difference in GLT-1 expression between Sham-Rac1^{wt} and Sham-Rac1KO. **C**, Fluorescent in situ hybridization (RNAscope) of *Gfap* and *Slc1A2* (GLT-1) mRNA in the ventral horn of the spinal cord in Sham-Rac1^{wt}, Sham-Rac1KO, SCI-Rac1^{wt}, and SCI-Rac1KO. Inset images are representative of a single *Gfap*+ nucleus. **D**, The expression of *Slc1a2* fluorescent puncta (i.e., mRNA transcripts) in *Gfap*+ nuclei in the ventral spinal cord compared between groups as a percentage of control (Sham-Rac1^{wt}) levels. SCI reduces the expression of *Slc1a2* mRNA compared to both Sham-Rac1^{wt} and Sham-Rac1KO. However, Rac1KO animals with SCI displayed higher levels of *Slc1a2* compared to SCI-Rac1^{wt} controls. **E**, Total number of *Gfap*+ nuclei normalized to the total number of nuclei within the ventral horn of the spinal cord compared as a percentage of control (Sham-Rac1^{wt}) levels. SCI induced an increase in the number of *Gfap*+ nuclei compared to the Sham control. In addition, there was no difference in *Gfap*+ nuclei between SCI-Rac1^{wt} and SCI-Rac1KO. Scale bar in **A** = 10 μ m and applies to images in **A**, scale bar in **C** = 50 μ m and applies to images in **C**, scale bar in **C** inset = 5 μ m and applies to all inset images in **C**. $n = 4$ per group, and graphs are mean \pm SEM ($*p < 0.05$).

paradigm, such observations have not been replicated in murine SCI models (Ryu et al., 2017). On the other hand, hindlimb reflex clasp behavior does emerge in a broad range of CNS disease models, including Huntington's disease, Alzheimer's Disease, Rett syndrome, multiple sclerosis, and hereditary spastic paraplegia (Lalonde and Strazielle, 2011; Cahill et al., 2019). The authors from these and other studies have speculated that the onset of hindlimb clasp behavior could potentially serve as an early indicator of spasticity following SCI (Qiang et al., 2019; Loy et al., 2021). The broad number of disease mechanisms associated with the hindlimb clasp behavior limits its use as a direct measure of spasticity. However, in combination with additional

behavioral testing, such as BMS and H-reflex, changes in the hindlimb clasp reflex may provide additional information about changes in motor function.

In our study, we did not observe any hindlimb clasp behavior in uninjured animals (i.e., Sham-Rac1^{wt} and Sham-Rac1KO). However, hindlimb clasp reflex was readily detectable at 2 and 3 weeks after SCI in Rac1^{wt} animals. Interestingly, our H-reflex testing results supported these clasp reflex observations, as we noted that animals with astrocytic Rac1KO exhibited a significant reduction in hindlimb clasp reflex compared to SCI-Rac1^{wt} animals. The clasp reflex is typically indicative of disruptions within the brain and spinal cord regions

responsible for motor control, with the specific presentation of this abnormal reflex behavior varying based on the type and severity of trauma or disease. Studies have shown that hindlimb claspings may indicate α -motor neuron malfunction within ventral spinal circuits and may be associated with axonal injury and demyelination (Dequen et al., 2010; Morgan et al., 2022; Scarrott et al., 2023). In our study, we observed a reduction in hindlimb reflex behavior with Rac1KO despite no obvious changes to overall motor recovery (e.g., BMS and open field). These findings suggest that there is a distinct difference in the underlying physiological mechanisms governing hindlimb claspings reflex and gross motor function following SCI.

Emerging evidence from other studies along with our present work suggests a distinct and divergent role for Rac1, depending on its tissue expression in astrocytes or neurons. We showed in prior studies that intrathecal administration of the Rac1 inhibitor, NSC23766, reduces *both* thin- and mushroom-shaped dendritic spines (Bandaru et al., 2015) and that conditional Rac1KO specifically from α -motor neurons, that is, in the cre-flox system, *only* reduced mushroom spine density and not thin spine density after SCI (Benson et al., 2021). Here, we show that conditional Rac1KO in astrocytes decreased *only* thin spines after SCI. Taken together, our current work extends our previous findings and shows that the context of Rac1 activity, for example, neuronal versus astrocytic, is important for understanding how Rac1 signaling operates within the injured spinal cord.

Mushroom-shaped dendritic spines serve as the primary morphological correlate of spinal circuit hyperexcitability (Bandaru et al., 2015; Yasuda, 2017). As such, we expected the observed normal density of mushroom spines in uninjured astrocytic Rac1KO animals—which did not present with any hindlimb claspings events and had normal gross locomotor function (Tan et al., 2009; Bosch and Hayashi, 2012). However, we did surprisingly observe in uninjured astrocytic Rac1KO animals a significant increase in thin-shaped spine density and an amplified H-reflex response at the 50 ms inter-pulse interval. Interestingly, after SCI in astrocytic Rac1KO animals, the initial elevated thin spine densities decreased, which suggests an involvement of astrocytes in a homeostatic process that maintains synaptic dendritic spine structure. Astrocytes regulate circuit function, in part through the elimination of immature or underutilized synaptic structures (Nguyen et al., 2011).

In agreement, Nishida and Okabe (2007) previously reported that astrocytic Rac1KO predominantly produced increased thin spine morphologies in hippocampal neurons (Nishida and Okabe, 2007). In this cortical study, the lack of astrocytic Rac1 impaired astrocyte motility, which prevented dendritic spine maturation via the loss of direct astrocyte-spine contact (Nishida and Okabe, 2007). Other studies have demonstrated that astrocytic Rac1KO impairs astrocyte-mediated phagocytosis, largely because Rac1 plays a crucial role in the rearrangement of the actin cytoskeleton, a process required for astrocytes to effectively engulf target structures (Lovatt et al., 2007; Cahoy et al., 2008; Loov et al., 2012; Ziegenfuss et al., 2012). In our present study, the absence of this Rac1-dependent phagocytotic process in astrocytic Rac1KO animals would have disrupted the removal of excess dendritic spines during CNS development. Here, a putative homeostatic mechanism that eliminates excess immature dendritic spines would only become apparent following SCI (Yu et al., 2008; Loov et al., 2012).

An important question arises from our study: How does astrocytic Rac1 activity contribute to hyperreflexia? Astrocytic dysfunction at synapses has been shown to alter glutamate concentration, leading to increased amplitude and length of NMDA postsynaptic potentials (Panatier et al., 2006; Valtcheva and Venance, 2019). Dysfunctional expression of GLT-1 in astrocytic peri-synaptic processes, which mediates the reuptake, clearance, and recycling of glutamate at the synaptic cleft, has been implicated in circuit hyperexcitability (Rothstein et al., 1994; Perego et al., 2000; Andersen et al., 2021). Indeed, poor clearance of glutamate can lead to hyperexcitability, excitotoxicity, and even abnormal synaptic morphology (Lewerenz and Maher, 2015; Olivares-Banuelos et al., 2019). For example, in an *Fmr1* KO mouse model of fragile X syndrome, astrocytes have reduced GLT-1 expression, and *fmr1*KO astrocytes induce abnormal synaptic morphology in cocultured hippocampal neurons (Higashimori et al., 2013). Global *Fmr1* KO also results in longer and thinner appearing dendritic spines in the cortex, an observation that matches our present findings in the ventral horn of astrocytic Rac1KO animals (Pyronneau et al., 2017).

In our study, we observed a significant increase in GLT-1 protein expression after SCI as compared with injured WT animals. In contrast, we observed that SCI led to a decrease in the astrocytic expression of *Slc1a2* (GLT-1) mRNA. To reconcile these seemingly contradictory findings, we examined whether there was a change in the number of astrocytes, by analyzing the number of *Gfap*⁺ nuclei in the ventral spinal cord after SCI. As expected, we detected an increase in the number of astrocytes within the ventral horn of the injured spinal cord tissue. Therefore, despite the decrease in per-astrocyte GLT-1 gene expression, the overall rise in the number of astrocytes could result in a net increase of GLT-1 within the spinal cord. Furthermore, while SCI induced a decrease in *Slc1a2* expression in both Rac1 WT and Rac1KO animals, astrocytes devoid of Rac1KO exhibited higher levels of *Slc1a2*. This amplified *Slc1a2* expression post-SCI could potentially account for the observed increase in GLT-1 protein within the SCI-Rac1KO group, as determined by immunolabeling techniques. This finding supports others' work revealing a direct interaction between astrocytic Rac1 and GLT-1 protein. Blocking Rac1 activity with NSC23766 enhanced GLT-1 activity and improved synaptic glutamate clearance in this model (Piniella et al., 2018). Overall, these observations along with our current report strongly implicate astrocytic Rac1 dysregulation in injury-induced amplification of synaptic excitability; postsynaptic structural reorganization, for example, dendritic spine dysgenesis; and the presentation of hyperreflexia.

In summary, this study shows for the first time that astrocytic Rac1 contributes to the presentation of spasticity after SCI. Specifically, astrocytic Rac1KO reduces injury-induced evoked H-reflex excitability, partly decreases dendritic spine dysgenesis on α -motor neurons, and elevates expression of homeostatic glutamate clearance mechanism, GLT-1. Taken together, this study supports a distinct role for astrocytic Rac1 signaling within the spinal reflex circuit. While much is still unknown about the mechanisms underlying spasticity, this study provides new insight into the potential role of astrocytes in this process.

References

- Andersen JV, Markussen KH, Jakobsen E, Schousboe A, Waagepetersen HS, Rosenberg PA, Aldana BI (2021) Glutamate metabolism and recycling at the excitatory synapse in health and neurodegeneration. *Neuropharmacology* 196:108719.

- Bandaru SP, Liu S, Waxman SG, Tan AM (2015) Dendritic spine dysgenesis contributes to hyperreflexia after spinal cord injury. *J Neurophysiol* 113:1598–1615.
- Bankhead P, et al. (2017) QuPath: Open source software for digital pathology image analysis. *Sci Rep* 7:16878.
- Basso DM, Fisher LC, Anderson AJ, Jakeman LB, McTigue DM, Popovich PG (2006) Basso mouse scale for locomotion detects differences in recovery after spinal cord injury in five common mouse strains. *J Neurotrauma* 23:635–659.
- Beaudet MJ, Yang Q, Cadau S, Blais M, Bellenfant S, Gros-Louis F, Berthod F (2015) High yield extraction of pure spinal motor neurons, astrocytes and microglia from single embryo and adult mouse spinal cord. *Sci Rep* 5:16763.
- Benson CA, Fenrich KK, Olson KL, Patwa S, Bangalore L, Waxman SG, Tan AM (2020) Dendritic spine dynamics after peripheral nerve injury: an intravital structural study. *J Neurosci* 40:4297–4308.
- Benson CA, Olson KL, Patwa S, Reimer ML, Bangalore L, Hill M, Waxman SG, Tan AM (2021) Conditional RAC1 knockout in motor neurons restores H-reflex rate-dependent depression after spinal cord injury. *Sci Rep* 11:7838.
- Blanco-Suárez E, Caldwell AL, Allen NJ (2017) Role of astrocyte–synapse interactions in CNS disorders. *J Physiol* 595:1903–1916.
- Bosch M, Hayashi Y (2012) Structural plasticity of dendritic spines. *Curr Opin Neurobiol* 22:383–388.
- Boulenguez P, Vinay L (2009) Strategies to restore motor functions after spinal cord injury. *Curr Opin Neurobiol* 19:587–600.
- Boulenguez P, et al. (2010) Down-regulation of the potassium-chloride cotransporter KCC2 contributes to spasticity after spinal cord injury. *Nat Med* 16:302–307.
- Broadhead MJ, et al. (2020) Nanostructural diversity of synapses in the mammalian spinal cord. *Sci Rep* 10:8189.
- Cahill LS, et al. (2019) Aged hind-limb claspings experimental autoimmune encephalomyelitis models aspects of the neurodegenerative process seen in multiple sclerosis. *Proc Natl Acad Sci U S A* 116:22710–22720.
- Cahoy JD, et al. (2008) A transcriptome database for astrocytes, neurons, and oligodendrocytes: a new resource for understanding brain development and function. *J Neurosci* 28:264–278.
- Crockett DP, Harris SL, Egger MD (1987) Plantar motoneuron columns in the rat. *J Comp Neurol* 265:109–118.
- Danbolt NC (2001) Glutamate uptake. *Prog Neurobiol* 65:1–105.
- Dequen F, Filali M, Lariviere RC, Perrot R, Hisanaga S, Julien JP (2010) Reversal of neuropathy phenotypes in conditional mouse model of Charcot-Marie-Tooth disease type 2E. *Hum Mol Genet* 19:2616–2629.
- Fan XC, Ma CN, Song JC, Liao ZH, Huang N, Liu X, Ma L (2021) Rac1 signaling in amygdala astrocytes regulates fear memory acquisition and retrieval. *Neurosci Bull* 37:947–958.
- Finnerup NB (2017) Neuropathic pain and spasticity: intricate consequences of spinal cord injury. *Spinal Cord* 55:1046–1050.
- Friese A, Kaltschmidt JA, Ladle DR, Sigrist M, Jessell TM, Arber S (2009) Gamma and alpha motor neurons distinguished by expression of transcription factor *Err3*. *Proc Natl Acad Sci U S A* 106:13588–13593.
- Guo Y, Benson C, Hill M, Henry S, Effraim P, Waxman SG, Dib-Hajj S, Tan AM (2018) Therapeutic potential of Pak1 inhibition for pain associated with cutaneous burn injury. *Mol Pain* 14:1744806918788648.
- Halpain S, Spencer K, Graber S (2005) Dynamics and pathology of dendritic spines. *Prog Brain Res* 147:29–37.
- Hebel R, Stromberg MW (1976) *Anatomy of the laboratory rat*. Baltimore: The Williams & Wilkins Company.
- Hefferan MP, et al. (2007) Spinal astrocyte glutamate receptor 1 overexpression after ischemic insult facilitates behavioral signs of spasticity and rigidity. *J Neurosci* 27:11179–11191.
- Higashimori H, Morel L, Huth J, Lindemann L, Dulla C, Taylor A, Freeman M, Yang Y (2013) Astroglial FMRP-dependent translational down-regulation of mGluR5 underlies glutamate transporter GLT1 dysregulation in the fragile X mouse. *Hum Mol Genet* 22:2041–2054.
- Ho SM, Waite PM (2002) Effects of different anesthetics on the paired-pulse depression of the h reflex in adult rat. *Exp Neurol* 177:494–502.
- Holtz KA, Lipson R, Noonan VK, Kwon BK, Mills PB (2017) Prevalence and effect of problematic spasticity after traumatic spinal cord injury. *Arch Phys Med Rehabil* 98:1132–1138.
- Hosoido T, Motoyama S, Goto M, Mori F, Tajima T, Hirata H, Wada N (2009) Characteristics of H- and M-waves recorded from rat forelimbs. *Neurosci Lett* 450:239–241.
- Ji RR, Strichartz G (2004) Cell signaling and the genesis of neuropathic pain. *Sci STKE* 2004:reE14.
- Ji RR, Donnelly CR, Nedergaard M (2019) Astrocytes in chronic pain and itch. *Nat Rev Neurosci* 20:667–685.
- Lalonde R, Strazielle C (2011) Brain regions and genes affecting limb-clasping responses. *Brain Res Rev* 67:252–259.
- Lance JW (1980) The control of muscle tone, reflexes, and movement: Robert Wartenberg Lecture. *Neurology* 30:1303–1313.
- Lee HJ, Jakovcevski I, Radonjic N, Hoelters L, Schachner M, Irintchev A (2009) Better functional outcome of compression spinal cord injury in mice is associated with enhanced H-reflex responses. *Exp Neurol* 216:365–374.
- Lewerenz J, Maher P (2015) Chronic glutamate toxicity in neurodegenerative diseases—what is the evidence? *Front Neurosci* 9:469.
- Loov C, Hillered L, Ebendal T, Erlandsson A (2012) Engulfing astrocytes protect neurons from contact-induced apoptosis following injury. *PLoS One* 7:e33090.
- Lovatt D, et al. (2007) The transcriptome and metabolic gene signature of protoplasmic astrocytes in the adult murine cortex. *J Neurosci* 27:12255–12266.
- Loy K, Fournau J, Meng N, Denecke C, Locatelli G, Bareyre FM (2021) Semaphorin 7A restricts serotonergic innervation and ensures recovery after spinal cord injury. *Cell Mol Life Sci* 78:2911–2927.
- Morgan ML, Teo W, Hernandez Y, Brideau C, Cummins K, Kuipers HF, Stys PK (2022) Cuprizone-induced demyelination in mouse brain is not due to depletion of copper. *ASN Neuro* 14:17590914221126367.
- Nguyen JV, et al. (2011) Myelination transition zone astrocytes are constitutively phagocytic and have synuclein dependent reactivity in glaucoma. *Proc Natl Acad Sci U S A* 108:1176–1181.
- Nielsen JB, Crone C, Hultborn H (2007) The spinal pathophysiology of spasticity—from a basic science point of view. *Acta Physiol (Oxf)* 189:171–180.
- Nishi RA, Liu H, Chu Y, Hamamura M, Su MY, Nalcioğlu O, Anderson AJ (2007) Behavioral, histological, and ex vivo magnetic resonance imaging assessment of graded contusion spinal cord injury in mice. *J Neurotrauma* 24:674–689.
- Nishida H, Okabe S (2007) Direct astrocytic contacts regulate local maturation of dendritic spines. *J Neurosci* 27:331–340.
- Olivares-Banuelos TN, Chi-Castaneda D, Ortega A (2019) Glutamate transporters: gene expression regulation and signaling properties. *Neuropharmacology* 161:107550.
- Palmieri RM, Ingersoll CD, Hoffman MA (2004) The Hoffmann reflex: methodological considerations and applications for use in sports medicine and athletic training research. *J Athl Train* 39:268–277. <https://www.ncbi.nlm.nih.gov/pmc/articles/PMC522151/>
- Panatier A, Theodosis DT, Mothet JP, Touquet B, Pollegioni L, Poulain DA, Olié SH (2006) Glia-derived D-serine controls NMDA receptor activity and synaptic memory. *Cell* 125:775–784.
- Patwa S, Benson CA, Dyer L, Olson KL, Bangalore L, Hill M, Waxman SG, Tan AM (2019) Spinal cord motor neuron plasticity accompanies second-degree burn injury and chronic pain. *Physiol Rep* 7:e14288.
- Perego C, Vanoni C, Bossi M, Massari S, Basudev H, Longhi R, Pietrini G (2000) The GLT-1 and GLAST glutamate transporters are expressed on morphologically distinct astrocytes and regulated by neuronal activity in primary hippocampal cocultures. *J Neurochem* 75:1076–1084.
- Peterson AR, Binder DK (2020) Astrocyte glutamate uptake and signaling as novel targets for antiepileptogenic therapy. *Front Neurol* 11:1006.
- Piniella D, Martinez-Blanco E, Ibanez I, Bartolome-Martin D, Porlan E, Diez-Guerra J, Gimenez C, Zafra F (2018) Identification of novel regulatory partners of the glutamate transporter GLT-1. *Glia* 66:2737–2755.
- Pyronneau A, He Q, Hwang JY, Porch M, Contractor A, Zukin RS (2017) Aberrant Rac1-cofilin signaling mediates defects in dendritic spines, synaptic function, and sensory perception in fragile X syndrome. *Sci Signal* 10:1–22.
- Qiang L, et al. (2019) Hereditary spastic paraplegia: gain-of-function mechanisms revealed by new transgenic mouse. *Hum Mol Genet* 28:1136–1152.
- Rodriguez A, Zhang HQ, Klaminder J, Brodin T, Andersson PL, Andersson M (2018) ToxTrac: a fast and robust software for tracking organisms. *Methods Ecol Evol* 9:460–464.
- Rothstein JD, Martin L, Levey AI, Dykes-Hoberg M, Jin L, Wu D, Nash N, Kuncl RW (1994) Localization of neuronal and glial glutamate transporters. *Neuron* 13:713–725.

- Ryu Y, et al. (2017) The swimming test is effective for evaluating spasticity after contusive spinal cord injury. *PLoS One* 12:e0171937.
- Savtchouk I, Volterra A (2018) Gliotransmission: beyond black-and-white. *J Neurosci* 38:14–25.
- Scarrott JM, Alves-Cruzeiro J, Marchi PM, Webster CP, Yang ZL, Karyka E, Marrocella R, Coldicott I, Thomas H, Azzouz M (2023) Ap4b1-knockout mouse model of hereditary spastic paraplegia type 47 displays motor dysfunction, aberrant brain morphology and ATG9A mislocalization. *Brain Commun* 5:fcac335.
- Scheff SW, Rabchevsky AG, Fugaccia I, Main JA, Lumpp JE Jr (2003) Experimental modeling of spinal cord injury: characterization of a force-defined injury device. *J Neurotrauma* 20:179–193.
- Schieppati M (1987) The Hoffmann reflex: a means of assessing spinal reflex excitability and its descending control in man. *Prog Neurobiol* 28:345–376.
- Skold C, Levi R, Seiger A (1999) Spasticity after traumatic spinal cord injury: nature, severity, and location. *Arch Phys Med Rehabil* 80:1548–1557.
- Stratton HJ, Khanna R (2020) Sculpting dendritic spines during initiation and maintenance of neuropathic pain. *J Neurosci* 40:7578–7589.
- Svensson M, Andersson E, Manouchehrian O, Yang Y, Deierborg T (2020) Voluntary running does not reduce neuroinflammation or improve non-cognitive behavior in the 5xFAD mouse model of Alzheimer's disease. *Sci Rep* 10:1346.
- Tan AM, Waxman SG (2012) Spinal cord injury, dendritic spine remodeling, and spinal memory mechanisms. *Exp Neurol* 235:142–151.
- Tan AM, Stamboulian S, Chang Y-W, Zhao P, Hains AB, Waxman SG, Hains BC (2008) Neuropathic pain memory is maintained by Rac1-regulated dendritic spine remodeling after spinal cord injury. *J Neurosci* 28:13173.
- Tan AM, Choi JS, Waxman SG, Hains BC (2009) Dendritic spine remodeling after spinal cord injury alters neuronal signal processing. *J Neurophysiol* 102:2396–2409.
- Tan AM, Chang YW, Zhao P, Hains BC, Waxman SG (2011) Rac1-regulated dendritic spine remodeling contributes to neuropathic pain after peripheral nerve injury. *Exp Neurol* 232:222–233.
- Tan AM, Chakrabarty S, Kimura H, Martin JH (2012) Selective corticospinal tract injury in the rat induces primary afferent fiber sprouting in the spinal cord and hyperreflexia. *J Neurosci* 32:12896–12908.
- Tenorio G, Kulkarni A, Kerr BJ (2013) Resident glial cell activation in response to perispinal inflammation leads to acute changes in nociceptive sensitivity: implications for the generation of neuropathic pain. *Pain* 154:71–81.
- Thompson FJ, Reier PJ, Lucas CC, Parmer R (1992) Altered patterns of reflex excitability subsequent to contusion injury of the rat spinal cord. *J Neurophysiol* 68:1473–1486.
- Valero-Cabre A, Fores J, Navarro X (2004) Reorganization of reflex responses mediated by different afferent sensory fibers after spinal cord transection. *J Neurophysiol* 91:2838–2848.
- Valtcheva S, Venance L (2019) Control of long-term plasticity by glutamate transporters. *Front Synaptic Neurosci* 11:10.
- Ventura R, Harris KM (1999) Three-dimensional relationships between hippocampal synapses and astrocytes. *J Neurosci* 19:6897–6906.
- Verhoog QP, Holtman L, Aronica E, van Vliet EA (2020) Astrocytes as guardians of neuronal excitability: mechanisms underlying epileptogenesis. *Front Neurol* 11:591690.
- Verkhatsky A, Nedergaard M (2018) Physiology of astroglia. *Physiol Rev* 98:239–389.
- Walter JS, Sacks J, Othman R, Rankin AZ, Nemchausky B, Chintam R, Wheeler JS (2002) A database of self-reported secondary medical problems among VA spinal cord injury patients: its role in clinical care and management. *J Rehabil Res Dev* 39:53–61. <https://pubmed.ncbi.nlm.nih.gov/11926327/>
- Wieters F, Weiss Lucas C, Gruhn M, Büschges A, Fink GR, Aswendt M (2021) Introduction to spasticity and related mouse models. *Exp Neurol* 335:113491.
- Yasuda R (2017) Biophysics of biochemical signaling in dendritic spines: implications in synaptic plasticity. *Biophys J* 113:2152–2159.
- Yu X, Lu N, Zhou Z (2008) Phagocytic receptor CED-1 initiates a signaling pathway for degrading engulfed apoptotic cells. *PLoS Biol* 6:e61.
- Yuste R, Majewska A, Holthoff K (2000) From form to function: calcium compartmentalization in dendritic spines. *Nat Neurosci* 3:653–659.
- Zeug A, Muller FE, Anders S, Herde MK, Minge D, Ponimaskin E, Henneberger C (2018) Control of astrocyte morphology by Rho GTPases. *Brain Res Bull* 136:44–53.
- Ziegenfuss JS, Doherty J, Freeman MR (2012) Distinct molecular pathways mediate glial activation and engulfment of axonal debris after axotomy. *Nat Neurosci* 15:979–987.